Monthly Notices
of the
ROYAL ASTRONOMICAL SOCIETY

MNRAS **489,** 5742–5763 (2019)
Advance Access publication 2019 September 11

doi:10.1093/mnras/stz2536

The prevalence of pseudo-bulges in the Auriga simulations

Ignacio D. Gargiulo,[1,2]★ Antonela Monachesi,[1,2] Facundo A. Gómez,[1,2] Robert J. J. Grand,[3] Federico Marinacci,[4] Rüdiger Pakmor,[3] Simon D. M. White,[3] Eric F. Bell,[5] Francesca Fragkoudi[3] and Patricia Tissera[6,7]

[1]*Instituto de Investigación Multidisciplinar en Ciencia y Tecnología, Universidad de La Serena, Raúl Bitrán 1305, La Serena, Chile*
[2]*Departamento de Física y Astronomía, Universidad de La Serena, Av. Juan Cisternas 1200 Norte, La Serena, Chile*
[3]*Max-Planck-Institut für Astrophysik, Karl-Schwarzschild-Str 1, D-85748, Garching, Germany*
[4]*Department of Physics and Astronomy, University of Bologna, via Gobetti 93/2, I-40129 Bologna, Italy*
[5]*Department of Astronomy, University of Michigan, 1085 S. University Avenue, Ann Arbor, MI 48109, USA*
[6]*Departamento de Ciencias Físicas, Universidad Andrés Bello, Fernandez Concha 700, Santiago, Chile*
[7]*Millennium Institute of Astrophysics, Fernandez Concha 700, Santiago, Chile*

Accepted 2019 September 5. Received 2019 September 4; in original form 2019 July 1

ABSTRACT

We study the galactic bulges in the Auriga simulations, a suite of 30 cosmological magneto-hydrodynamical zoom-in simulations of late-type galaxies in Milky Way sized dark matter haloes performed with the moving-mesh code AREPO. We aim to characterize bulge formation mechanisms in this large suite of galaxies simulated at high resolution in a fully cosmological context. The bulges of the Auriga galaxies show a large variety in their shapes, sizes, and formation histories. According to observational classification criteria, such as Sérsic index and degree of ordered rotation, the majority of the Auriga bulges can be classified as pseudo-bulges, while some of them can be seen as composite bulges with a classical component; however, none can be classified as a classical bulge. Auriga bulges show mostly an *in situ* origin, 21 per cent of them with a negligible accreted fraction ($f_{\rm acc} < 0.01$). In general, their *in situ* component was centrally formed, with ∼75 per cent of the bulges forming most of their stars inside the bulge region at $z = 0$. Part of their *in situ* mass growth is rapid and is associated with the effects of mergers, while another part is more secular in origin. In 90 per cent of the Auriga bulges, the accreted bulge component originates from less than four satellites. We investigate the relation between the accreted stellar haloes and the bulges of the Auriga simulations. The total bulge mass shows no correlation with the accreted stellar halo mass, as in observations. However, the accreted mass of bulges tends to correlate with their respective accreted stellar halo mass.

Key words: methods: numerical – galaxies: bulges – galaxies: formation.

1 INTRODUCTION

Milky Way (MW)-mass disc galaxies exhibit a large range of bulge properties and sizes, from prominent (e.g. M31), to almost non-existing bulges (e.g. M101). The diversity in the properties of these galaxies reveals the existence of different formation paths in the context of the current hierarchical galaxy formation paradigm (White & Rees 1978), which are not fully understood. The study of bulges of MW-sized galaxies in cosmological simulations is then an important task to try to explain the observed properties of the MW and luminous disc galaxies.

Galactic bulges are broadly classified as classical bulges or pseudo-bulges. Historically, the classical bulges were defined as velocity dispersion-dominated components in the centre of disc galaxies. These objects have old stellar populations, exhibit a slow degree of rotation, and present a spherical or elliptical shape. Yet, many bulges show rotation, younger stellar populations, and different features related to a disc-origin, like spiral structure, or nuclear bars. These differences have led to suggestions that such bulges (including bars) should be grouped and termed pseudo-bulges (see Kormendy & Kennicutt 2004, for a historical review on the subject). In the last decade, it has become increasingly clear that a large fraction of disc galaxies in the local Universe hosts pseudo-bulges (Gadotti 2009; Kormendy et al. 2010; Fisher & Drory 2011, 2016; Kormendy & Bender 2019). Fisher & Drory (2011) found,

★ E-mail: ignacio.gargiulo@gmail.com

in a volume-limited sample within 11 Mpc, that 80 per cent of disc galaxies with stellar masses larger than 10^9 $M_\odot$ have pseudo-bulges or are bulgeless. Moreover, it has been determined in the last few years that MW-analogues commonly lack a classical bulge component, or if there is one, it is not dominant. Kormendy et al. (2010) found that 11 out of 19 massive disc galaxies in the local Universe do not possess a classical bulge. In a recent paper, Kormendy & Bender (2019) showed that two nearby MW-like galaxies (NGC 4565 and NGC 5746) host also a pseudo-bulge with similar properties to the MW-bulge and without signs of the presence of a classical bulge. Observations and models of the MW itself indicate that a classical bulge component must be inconspicuous, if present (Shen et al. 2010; Di Matteo et al. 2015; Debattista et al. 2017; Gómez et al. 2018). Since, historically, classical bulges are considered to be formed in minor to intermediate mergers in a process analogous to that of the formation of elliptical galaxies (Kauffmann, White & Guiderdoni 1993), this apparent low frequency of classical bulges in large disc galaxies has led some authors to claim a tension with the hierarchical clustering paradigm, where the formation of large galaxies should involve a relatively high amount of mergers. However, analysis performed on single cosmological simulations, or small samples of them, suggests that the formation of pseudo-bulges is not infrequent. Guedes et al. (2013) used a simulation of a late-type galaxy, Eris (Guedes et al. 2011), to study the formation of its pseudo-bulge and found that most of the mass in the pseudo-bulge was formed in a bar configuration at high redshift that was later reshaped into a dense flattened structure and inner bar. Okamoto (2013) studied the formation channels of two pseudo-bulges in hydrodynamical resimulations of the Aquarius DM haloes (Springel et al. 2008) and found that both of them formed at high redshift by means of the accretion of misaligned gas, with secular evolution contributing to less than 30 per cent of the final mass of the pseudo-bulges. Debattista et al. (2019) studied in detail a high spatial and force resolution simulation from the FIRE project (Wetzel et al. 2016) with signatures of *kinematic fractionation* (Debattista et al. 2017) during its bar evolution, a phenomenon that can explain the observed properties of the MW bulge without the need of significant merger contributions to its formation. Under this scenario, stellar populations with different kinematic properties at birth in barred galaxies end-up with different spatial distributions (see also Fragkoudi et al. 2017). Buck et al. (2018, 2019) studied the inner region of an MW-like galaxy simulation and found two populations with distinct kinematics; one of them rapidly rotating and the other without significant rotation. Interestingly both populations formed mostly *in situ*, with different initial angular momenta. Despite these results already suggest that the formation of pseudo-bulges in simulated disc galaxies, within a ΛCDM framework, is common, the frequency with which classical and pseudo-bulges form has not yet been addressed for MW-sized galaxies (see, although, Rosito et al. (2019) where is found that 85 per cent of spheroid dominated galaxies in the EAGLE simulation have Sérsic indices $n < 2$). This is due to the lack of a large and homogeneous sample of simulated galaxies with enough resolution to study the detailed structure of the stellar component in the inner few kiloparsecs. One of the goals of this paper is to survey the properties of bulges in one of the largest samples of high-resolution hydrodynamical simulations of MW-mass galaxies, evolved in a cosmological context; namely the Auriga project (Grand et al. 2017, G2017 from now on). We wish to find the relative frequency of classical and pseudo-bulge formation.

MW-analogues in the local Universe, where most of the bulges are found to be pseudo-bulges, present a great diversity in its accretion histories, as revealed by detailed observations and determinations of properties of their stellar haloes (Monachesi et al. 2016; Harmsen et al. 2017), which is also seen in simulations (D'Souza & Bell 2018b; Monachesi et al. 2019). It is not clear, however, under which conditions the accretion events that are involved in the build-up of the stellar halo contribute to the formation of the bulge, if they are involved at all (Bell et al. 2017). The second goal of this paper is to study the origin and formation history of galactic bulges, and relate their properties to the properties of the corresponding stellar haloes presented in Monachesi et al. (2019, M2019 hereafter). This paper is organized as follows. In Section 2 we describe the simulations used in this work and present the definition of the Auriga stellar bulges. In Section 3 we present the structural properties of the bulges and compare them with observational data. In Section 4 we study the formation history of the Auriga bulges, we define their *in situ* and accreted components and present the results and analysis for each component separately. We dedicate a subsection to study the relation of the Auriga bulges and their stellar haloes. Section 5 is devoted to the discussion of the results and Section 6 presents our summary and conclusions.

2 METHODOLOGY

2.1 The Auriga simulations

The Auriga simulations consist of a suite of 30 high-resolution cosmological zoom simulations of the formation of galaxies in isolated MW-mass dark matter haloes, denoted throughout this paper by 'AuN' with N varying from 1 to 30. The Auriga project was introduced in G2017 and we refer the reader to that paper for a detailed description of these simulations. Here, we briefly describe their main features.

Candidate haloes were selected from a lower resolution dark matter only cosmological simulation from the EAGLE project (Schaye et al. 2015), carried out in a periodic cube of side $100\,h^{-1}$ Mpc. A ΛCDM cosmology was adopted, with parameters $\Omega_\mathrm{m} = 0.307$, $\Omega_\mathrm{b} = 0.048$, $\Omega_\Lambda = 0.693$, and Hubble constant $H_0 = 100\,h$ km s^{-1} Mpc^{-1}, $h = 0.6777$ (Planck Collaboration XVI 2014). Gas was added to the initial conditions and its evolution was followed by solving the equations of ideal magnetohydrodynamics on an unstructured Voronoi mesh. Haloes were selected so that they satisfy: (a) a narrow mass range of $1 < M_{200}/10^{12}\,\mathrm{M}_\odot < 2$, comparable to that of the MW and (b) an isolation criterion at $z = 0$, placing each Auriga halo more distant than nine times its virial radius from any other halo of mass greater than 3 per cent of its own mass. Each halo was re-simulated at higher resolution with the state-of-the-art *N*-body and moving mesh magnetohydrodynamics code AREPO (Springel 2010; Pakmor et al. 2016). The typical mass of a dark matter particle is $\sim 3 \times 10^5$ $\mathrm{M}_\odot$, and the baryonic mass resolution is $\sim 5 \times 10^4$ $\mathrm{M}_\odot$. The gravitational softening length of the stars and dark matter grows with the scale factor up to a maximum of 369 pc, after which it is kept constant in physical units. This value is large enough to resolve inner galactic regions. As shown by GR2017, decreasing the softening lenght by a factor of 10 does not affect the overall properties of the resulting galactic models. The softening length of gas cells is scaled by the mean radius of the cell, with a maximum physical softening of 1.85 kpc and is never allowed to drop below the stellar softening length. It is worth noting that, in high-density regions, gas cells are allowed to become smaller than the gravitational softening length. This is particularly relevant for this study, where we will be focusing in the very inner regions of each simulated galaxy. However, it is important to keep

in mind that our results could be sensitive to the subgrid physic model implemented in Auriga.

The simulations include a comprehensive model for galaxy formation physics which includes relevant baryonic processes, such as primordial and metal-line cooling (Vogelsberger et al. 2013); a sub-grid model for the interstellar medium (ISM) that utilizes an equation of state representing a two-phase medium in pressure equilibrium (Springel & Hernquist 2003); a model for the star formation and stellar feedback that includes a phenomenological wind model (Marinacci, Pakmor & Springel 2014; Grand et al. 2017) and metal enrichment from SNII, SNIa, and AGB stars (Vogelsberger et al. 2013); black hole formation and active galactic nucleus feedback (Springel, Di Matteo & Hernquist 2005; Marinacci et al. 2014; Grand et al. 2017); a spatially uniform, time-varying UV background after reionization at redshift six (Faucher-Giguère et al. 2009; Vogelsberger et al. 2013) and magnetic fields (Pakmor & Springel 2013; Pakmor, Marinacci & Springel 2014). Stellar particles are formed in AREPO out of the cold-gas phase of a two-phase ISM (Springel & Hernquist 2003). When a gas cell enters the thermally unstable star-forming regime, defined for gas densities higher than a density threshold, stellar particles are allowed to form. Gas cells are turned into stellar particles stochastically, with a probability consistent with their star formation rate. If the gas cell holds less than twice the target mass defined as $m_{\rm target} = m_{\rm b}$, where the mean baryonic mass, $m_{\rm b} \sim 5 \times 10^4$, all its mass is converted into stellar particles. Otherwise, only an amount of gas equal to the target mass is converted into stellar particles and the cell remains with the rest of the gas mass. Please note that a stellar particle in the Auriga simulations represents a co-eval, single metallicity stellar population following a Chabrier (2001) initial mass function. For a more detailed explanation, we defer the reader to Grand et al. (2017). The model was specifically developed for the AREPO code and was calibrated to reproduce several observational results such as the stellar mass to halo mass relation, galaxy luminosity functions, and the history of the cosmic star formation rate density.

The Auriga simulations reproduce a wide range of present-day observables, e.g. two-component disc-dominated galaxies with appropriate stellar masses, sizes, rotation curves, star formation rates, and metallicities (G2017). The relatively large sample of 30 high-resolution simulations of late-type galaxies is an ideal set of simulations to study bulge formation in MW-sized galaxies and to relate our findings to both the accretion history of these galaxies and their stellar bulge properties. It is worth noting that the above described isolation criterion may bias the number and timing of encounters with satellite galaxies with respect to more dense environments. Late time mergers may be less common on average in the sample used in this paper, with respect to a random sample of MW-sized DM haloes. However, these galaxies have not been specifically chosen to match the MW formation and merger history (as in e.g. Bullock & Johnston 2005) or the Local Group environment (as in the APOSTLE simulations of Sawala et al. 2016). Thus it is unclear how large this effect could be. We defer this analysis to a follow-up project based on the Illustris TNG50 simulations (Gargiulo et al., in preparation).

Throughout this paper, particle positions and velocities are defined in a different rotated reference system for each galaxy, such that discs are aligned with the *XY*-plane. We compute the total angular momentum of particles younger than 5 Gyr in the inner regions of the galaxy and rotate the particle positions and velocities in order to align the total angular momentum vector with the *Z*-axis of the rotated system. We repeat this procedure until convergence following Gómez et al. (2016b).

2.2 Bulge definition

Bulges of galaxies are defined in diverse ways in the literature, both in numerical simulations and observations. Observational studies often consider a spatial definition, selecting a region surrounding the center of the galaxy to some extent (see for example Minniti et al. 2010, for an MW bulge aimed survey). On the other hand, in numerical studies bulges are typically selected kinematically, to minimize the contribution of stars with orbits that are too circular, thus associated with the disc (e.g. Tissera, White & Scannapieco 2012; Guedes et al. 2013). It is also common to limit the spatial extent of the bulge to separate it from the stellar halo component, even though this is not a physical criterion to determine where the bulge ceases to exist and gives place to the so-called inner halo. For example, Cooper et al. (2015) and M2019 choose a spherical region of 5 kpc from the galactic center to mark the frontier between stellar halo and bulge. Other authors choose to avoid this spatial segregation, analysing the overall 'central spheroids' (Tissera et al. 2018).

Here we use a combination of a spatial and a kinematical criteria. We define the bulges of the Auriga simulations as all the stellar particles that fulfill the following two conditions at $z = 0$. First, we consider the particles located inside a sphere of radius $r_{\rm bulge} = 2R_{\rm eff}$, where $R_{\rm eff}$ is the effective radius of the bulge and was derived from a Sérsic profile fitting. The Sérsic profiles are fitted together with an exponential profile (modeling the disc) to the face-on Auriga surface brightness profiles in the *V*-band derived using a non-linear least-square method. The full process is described in Appendix A.

Secondly, we exclude stellar particles with pure disc kinematics. For that purpose, we consider only particles with circularities $|\epsilon| \leq 0.7$. The circularity parameter for the stellar particles at $z = 0$ was calculated by G2017. It is defined as $\epsilon = J_z/J(E)$ (Abadi et al. 2003), where J_z is the angular momentum component perpendicular to the disc plane of a star particle and $J(E)$ is the maximum possible angular momentum for the orbital energy, E, for the same particle. The median of the mass removed from the region defined as the bulge due to this circularity cut, for all Auriga simulations, is $m_{f_{\epsilon>0.7}} = 0.19$. Only for Au25 the total mass removed within $2R_{\rm eff}$ reaches almost 45 per cent. The total mass removed from each galaxy in this bulge defined region due to the circularity cut is listed in Table 1, along with other derived properties of the Auriga bulges. It is important to note that, when comparing with observations, the bulge is defined as closely as possible as it is done in the particular observational analysis. The goal is to make fair comparisons with the observed quantities in each particular case.

3 STRUCTURAL PROPERTIES OF BULGES

In Fig. 1 we show the edge-on projected surface brightness maps in the *V* band of the stellar particles that form the bulges. These were obtained by computing the photometry of each stellar particle, which represents a single stellar population, using Bruzual & Charlot (2003) population synthesis models. In the corners of each panel, we show the simulation name, the Sérsic index, and the bulge-to-total stellar mass ratio ($B/T_{\rm sim}$).

The bulges show an interesting diversity in morphology. While some of them show a more rounded or elliptical morphology, there are some clear peanut/boxy (p/b) or X-shaped bulges like Au17, Au18, or Au26. Perhaps the most interesting example is Au18, which shows an X-shape that resembles the morphology of the MW bulge (McWilliam & Zoccali 2010; Nataf et al. 2010). We note here that taking a more restrictive limit in the circularity cut

Table 1. Table of bulge parameters at $z = 0$. The columns are (1) model name; (2) bulge stellar mass, defined as the sum of all stellar particles inside the bulge region defined in Section 2.2; (3) Sérsic Index; (4) bulge-to-total ratio computed as the ratio between the sum of masses of particles inside bulges as defined in Section 2.2 and the sum of the masses of all stellar particles inside $0.1 \times R_{\rm vir}$; (5) bulge-to-total ratio derived from two-component fits to the surface brightness profile in the *V* band; (6) bulge effective radius; (7) accreted bulge fraction; (8) minor-to-major axial ratio *c*/*a*; (9) intermediate-to-major axial ratio *b*/a; (10) percentage of *in situ* bulge stars formed outside the bulge region; (11) fraction of *in situ* (all) stars younger than 8 Gyr; (12) fraction of stars inside the bulge region with circularities $\epsilon > 0.7$.

Sim	$\frac{M_{\rm bulge}}{[10^{10}\,{\rm M}_\odot]}$	$n_{\rm v}$	$\rm B/T_{sim}$	$\rm B/T_v$	$\frac{r_{\rm eff_v}}{[\rm kpc]}$	$f_{\rm acc}$	*c*/*a*	*b*/*a*	$f_{>2\rm Reff}$ (per cent)	$f_{<8\rm Gyr}$	$f_{\epsilon>0.7}$
Au1	1.01	1.26	0.37	0.24	1.24	–	0.73	0.77	–	–	0.25
Au2	1.36	1.32	0.19	0.07	1.40	0.15	0.72	0.78	33.1	0.37 (0.36)	0.15
Au3	1.55	1.30	0.20	0.11	1.72	0.23	0.89	0.98	17.9	0.11 (0.09)	0.32
Au4	1.53	1.65	0.21	0.12	1.62	0.42	0.92	0.99	42.9	0.93 (0.81)	0.25
Au5	1.31	0.82	0.19	0.09	0.68	<0.01	0.86	0.90	42.8	0.52 (0.51)	0.23
Au6	1.00	1.68	0.21	0.11	2.13	0.14	0.81	0.94	31.5	0.38 (0.33)	0.36
Au7	1.01	1.35	0.21	0.10	1.02	0.20	0.81	0.87	36.3	0.94 (0.79)	0.20
Au8	0.58	1.46	0.19	0.12	2.00	0.15	0.84	0.94	40.9	0.31 (0.33)	0.24
Au9	2.01	1.25	0.33	0.18	1.02	0.03	0.67	0.70	41.2	0.46 (0.45)	0.15
Au10	1.97	0.88	0.33	0.25	0.67	<0.01	0.68	0.73	56.8	0.74 (0.74)	0.15
Au11	1.83	1.10	0.26	0.41	1.34	–	0.65	0.69	–	–	0.16
Au12	0.83	0.60	0.14	0.07	0.60	0.01	0.76	0.81	53.1	0.71 (0.71)	0.16
Au13	2.10	1.18	0.34	0.53	0.95	0.01	0.71	0.74	51.1	0.79 (0.78)	0.18
Au14	1.88	1.14	0.18	0.12	0.75	0.02	0.75	0.80	46.1	0.74 (0.72)	0.18
Au15	0.27	0.64	0.07	0.03	0.62	0.02	0.88	0.99	52.1	0.84 (0.82)	0.24
Au16	0.65	1.20	0.12	0.05	1.44	0.01	0.85	0.96	31.9	0.18 (0.18)	0.35
Au17	3.41	0.88	0.45	0.49	1.06	<0.01	0.71	0.75	51.6	0.58 (0.58)	0.17
Au18	1.95	1.01	0.24	0.19	0.98	<0.01	0.78	0.81	57.4	0.52 (0.52)	0.16
Au19	1.07	1.94	0.20	0.13	1.39	0.22	0.90	0.99	32.3	0.71 (0.69)	0.24
Au20	1.35	1.85	0.28	0.13	1.51	0.18	0.72	0.77	33.0	0.32 (0.38)	0.14
Au21	1.03	1.08	0.13	0.13	1.08	0.10	0.82	0.91	38.2	0.74 (0.69)	0.26
Au22	1.90	0.81	0.31	0.20	0.72	<0.01	0.80	0.89	51.5	0.60 (0.60)	0.19
Au23	2.35	1.26	0.26	0.17	1.33	0.03	0.73	0.76	47.6	0.52 (0.50)	0.15
Au24	1.90	1.65	0.29	0.13	1.06	0.01	0.65	0.67	29.8	0.28 (0.28)	0.15
Au25	0.55	1.88	0.17	0.09	2.29	0.08	0.83	0.97	32.2	0.30 (0.28)	0.44
Au26	4.10	1.10	0.37	0.62	1.00	0.11	0.72	0.75	51.8	0.77 (0.68)	0.22
Au27	1.52	1.09	0.16	0.07	0.84	0.05	0.75	0.79	37.9	0.32 (0.31)	0.17
Au28	4.03	1.63	0.38	0.42	1.49	0.24	0.75	0.80	51.8	0.87 (0.76)	0.19
Au29	1.67	1.21	0.18	0.20	0.86	0.28	0.84	0.91	34.9	0.52 (0.50)	0.16
Au30	1.26	1.32	0.29	0.47	1.71	0.16	0.84	0.96	40.7	0.80 (0.74)	0.36

in the definition of galactic bulges (e.g. $|\epsilon| \leq 0.6$ instead of $|\epsilon| \leq 0.7$) does not significantly affect our results. Disc-like features of bulges are present even with a more stringent circularity threshold. Understanding the origin of this diversity is one of the aims of this study and a series of subsequent papers.

The Sérsic index was extracted from the same profile used to define the effective radius, discussed in the Appendix A. B/T was computed in two different ways. First, we computed $\rm B/T_{sim}$ as the ratio between the total mass of the stellar particles inside the bulge region as defined in the previous section and the total mass of the stellar particles inside a sphere of $0.1\times$ the virial radius of the host. In addition, we estimated the $\rm B/T_v$ from the two-component fit described in Appendix A. We integrated the fitted Sérsic function and divided the result by the integral of the sum of the Sérsic function and the exponential function describing the disc. The resulting B/T for all simulations using each method are shown in Table 1. We find that for all of the Auriga bulges $\rm B/T_{sim} < 0.5$ and most of the Auriga bulges, $\rm B/T_v < 0.5$, which is a common threshold above which the presence of a classical bulge is ensured, in observational studies (Brooks & Christensen 2016; Kormendy 2016). However, in some cases, observed bulges can be classified as classical even if the galaxy shows a low B/T (Fisher & Drory 2011). Au13 and Au26 show values of luminosity-weighted $\rm B/T_v > 0.5$. One of the reasons for this result is that these simulated galaxies experienced high levels of star formation in the last snapshots of the simulation (see the star formation histories in Figs 7 and 8 in Section 4.2). In the case of Au13, the surface brightness profile shows a prominent bump due to the bar that was extracted during the fitting procedure, but high levels of bar contamination in the light profile remain. Light profile decompositions of barred Auriga galaxies adding a third component for the bar show B/T below 0.5 for Au13 and Au26 (Blazquez-Calero et al., private communication). The effective radii of bulges vary from $R_{\rm eff} = 0.6$ kpc for Au12, to $R_{\rm eff} = 2.29$ kpc for Au25. The Sérsic indexes have values between $n = 0.6$ for Au12 and $n = 1.88$ for Au15. A list of bulge parameters presented here can be found in Table 1.

The photometric classification of observed galactic bulges as classical or pseudo-bulges can be difficult. The most straightforward approach is using the Sérsic index, which has been shown to correlate with bulge type. Fisher & Drory (2008) studied the bulges of 79 spiral galaxies observed with the *Hubble Space Telescope* (*HST*) spanning a range of morphologies from early-type to late-type. They found a bi-modal distribution of Sérsic index and showed that more than 90 per cent of the bulges that are classified as pseudo-bulges morphologically by visual inspection, have Sérsic

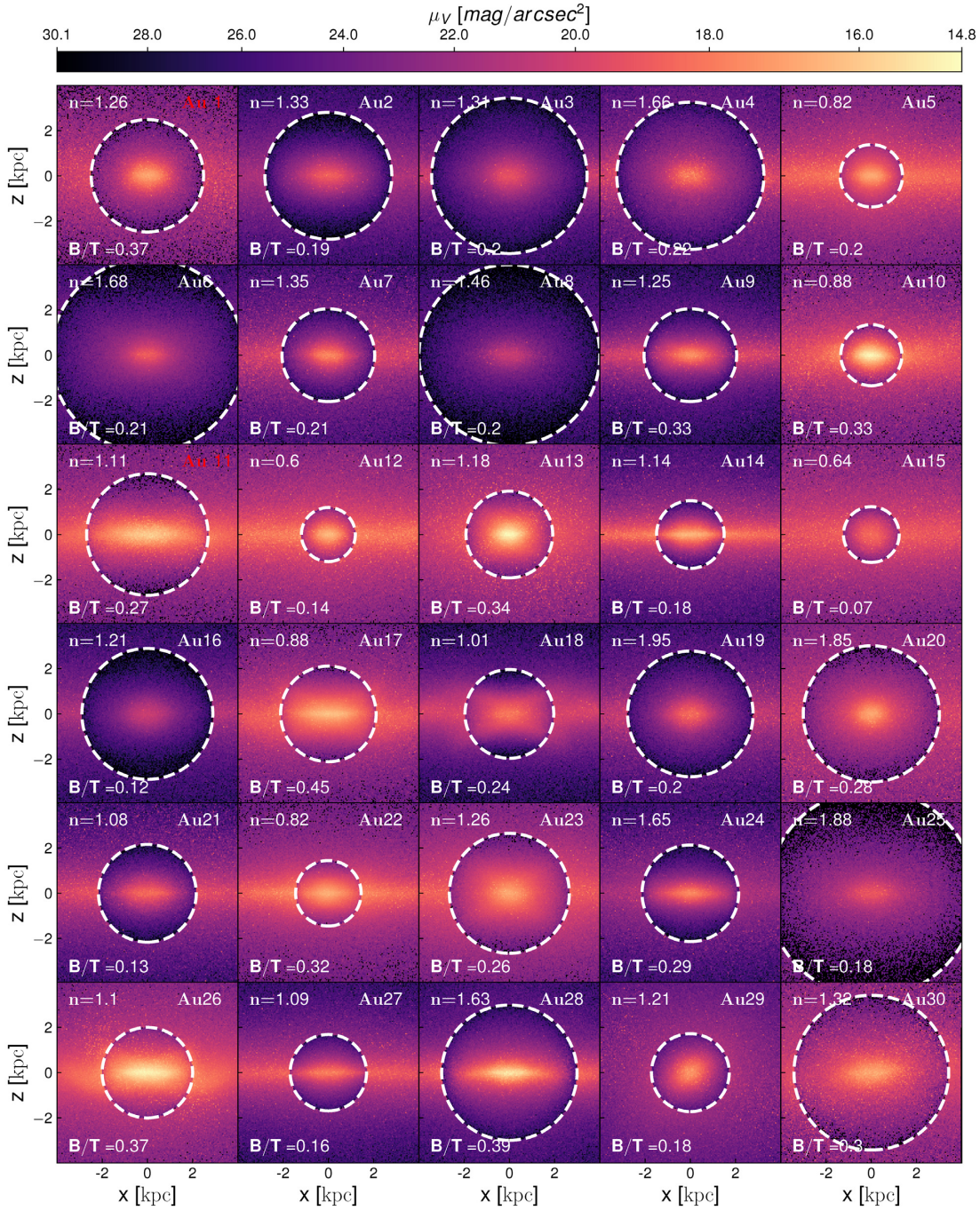

Figure 1. Projected *V*-band surface brightness maps of the Auriga bulges shown edge-on at $z = 0$ in a square region of 8 kpc on each side, centred in the galaxy. Bulges are defined using both an spatial and kinematic criteria (see text for details on the bulge definition in this work). The dashed white circle represents the bulge region within $2R_{\rm eff}$. Note that surface brightness beyond such circle is shown for all stellar particles, i.e. no kinematical cut. In the upper right corner of each panel the model name is shown. In the upper left corner the Sérsic index and in the lower left corner the bulge-to-total ratio.

indices $n \lesssim 2$. On the other side, classical bulges have commonly Sérsic indices $n > 2$. The dependence of this structural parameter with bulge type was already suggested in previous studies, such as Kormendy & Kennicutt (2004, and references therein). But it was also proven that using the Sérsic index as the only parameter of bulge classification can be too simplistic. Fisher & Drory (2011) used a combination of Sérsic index, morphological classification by visual inspection, and star formation activity to discriminate between bulge types and found that for composite bulges (those which show a distinguishable spheroidal classical component and, at the same time, show pseudo-bulge morphological features such as central spiral patterns, a ring or bar), the use of structural parameters as Sérsic index are not reliable.

If we only consider the Sérsic index parameter to classify the bulges, we find that all of the Auriga bulges should be classified as pseudo-bulges, i.e. $n < 2$. Yet, as previously highlighted (see also Kormendy 2016) a multiparameter classification must be carried out to reduce the error in bulge classification. In the following we

analyse the scaling relations, intrinsic shapes and degree of ordered rotation of the Auriga bulges.

3.1 Scaling relations

Scaling relations of bulges can be used as a complementary tool to help in the bulge classification. Gadotti (2009) used the relation between effective radius and surface brightness at the effective radius of elliptical galaxies, known as the Kormendy diagram (Kormendy 1977), as another way to determine the bulge type. They assumed that all galaxies outside 1σ of the relation followed by elliptical galaxies can be considered pseudo-bulges, but again Fisher & Drory (2011) showed that many pseudo-bulges selected morphologically can lie in the same region than classical bulges on this diagram and that this criterion cannot be used in isolation to determine a single bulge type. Yet, pseudo-bulges and classical bulges do show different behaviours in this diagram when seen as different samples. In Fig. 2 we show scaling relations of the bulges for the Auriga galaxies. In the upper panel, we show the Kormendy diagram. In the middle panel, we present the relation between the absolute magnitude in the V band and the surface brightness at the effective radius and in the bottom panel, we present the relation between absolute magenitude and sersic index. The Auriga bulges are indicated with black diamonds. Observational data from Fisher & Drory (2008) of classical bulges, pseudo-bulges, and elliptical galaxies are shown as green circles, red pentagons, and blue triangles, respectively. Average error bars of the observed data are indicated in a lower corner of the panels. To make a fair comparison with observations, in these diagrams all the quantities are derived directly from the two-component decomposition of the V-band surface brightness profiles (see Appendix A), without applying the kinematic cut previously defined in Section 2.2. Hence, M_V and μ_e values also include the contribution from particles with circular orbits inside the effective radius. It is expected that classical bulges follow the relation found for ellipticals, but pseudo-bulges usually show a larger scatter in these diagrams. In the Kormendy diagram (upper panel), the Auriga bulges occupy a rather narrow range in effective radii and appear to be systematically larger than the observed pseudo-bulges. While some simulated pseudo-bulges have similar sizes to the observed ones, the high surface brightness objects ($\mu_e < 17$ mag arsec^2) tend to be larger than observed. In general, we find that the Auriga bulges show a correlation in this diagram, with larger effective radii for smaller surface brightness. However, the slope shown by the Auriga bulges in the $\log(r_{\rm eff})$–$\mu_{\rm eff}$ relation is flatter than the slope shown by the observed clasical bulges or elliptical galaxies. Observed pseudo-bulges in this diagram show little to no-correlation.

In the middle panel of Fig. 2 we show the M_V–$\mu_{\rm eff}$ relation. While elliptical galaxies and classical bulges follow the same trend in this space, i.e. more luminous ellipticals and classical bulges are less centrally concentrated, the bulges of Auriga follow an opposite trend. The observed pseudo-bulges in this panel only show a large scatter. However, the results for the extended sample of galaxies with pseudo-bulges presented in Fisher & Drory (2011) follows qualitatively the same trend seen for the Auriga bulges, i.e. the more luminous the denser, as highlighted by the authors of that work (see their fig. 8).[1] A group of Auriga bulges (23 per cent of the total), namely Au10, Au11, Au13, Au14, Au17, Au26, Au28,

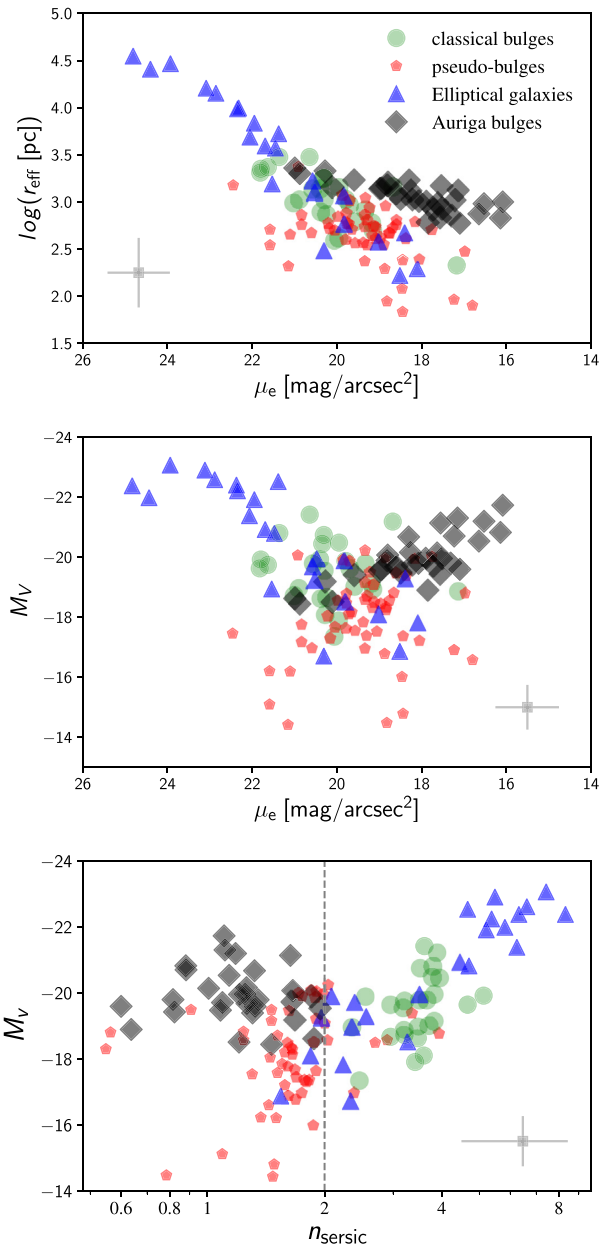

Figure 2. *Top:* Effective radii of galactic bulges as a function of surface brightness at effective radii in the V band. The Auriga bulges are indicated with black diamonds. Red pentagons, blue triangles, and green circles are observational data from (Fisher & Drory 2008). The grey square with error bars represents the averaged errors of the observations. *Middle:* Absolute magnitude as a function of surface brightness at the effective radius in the V band. *Bottom:* Absolute magnitude as a function of sersic index. The limit $n = 2$ is indicated with a dashed vertical line. All the Auriga bulges show $n < 2$.

show to be more luminous than any observed pseudo-bulge and present a higher surface brightness than most observed pseudo- and classical bulges of this sample. In the bottom panel of Fig. 2, we show the relation between M_V and sersic index. We can see that the sersic index of observed classical bulges follow broadly the relation

[1]Results in this paper are not quantitatively compared with observations in Fisher & Drory (2011) because they used images with filters centred at 3.6μ from the *Spitzer telescope*, which are not comparable with the available magnitudes in the Auriga simulations.

found for elliptical galaxies and observed pseudo-bulges show a large scatter with no signs of correlation. Although a group of the Auriga bulges show absolute magnitudes that are comparable with those of classical bulges, as already shown in the M_V–μ_{eff} relation, their sersic index and total magnitude are not correlated.

There are two points to take into account in the comparison with these set of observations. (i) Fisher & Drory (2008) exclude from the analysis the central regions of the surface brightness profiles when they identify a nuclei and due to resolution limits we cannot identify substructure in the underlying peak of surface brightness produced by the bulge component (see Appendix A). (ii) Additionally, extinction by dust is neglected in the simulations. Because of these two caveats, the total magnitudes of the Auriga bulges may be overestimated compared with the observed ones. Besides, this group of galaxies with higher absolute magnitudes in the *V* band are all actively forming stars in the last snapshots of the simulation (as can be seen in Figs 7 and 8). As discussed in Section 5, simulated stellar feedback might not suppress enough star formation in this set of simulations, thus likely generating more massive simulated bulges. It is worth also noting that the observational sample contains the whole range of disc galaxy morphologies and, most likely, a wider range in DM halo masses without any environmental selection criterion. Our simulations are restricted to a narrow range of DM haloes ($1–2 \times 10^{12}$ $M_\odot$) and are selected with an isolation criterion as explained in Section 2. Note also that, as shown by Fisher & Drory (2011), a reliable classification of a bulge into either pseudo or classical cannot be done only with the object position in the Kormendy diagram. Instead, all available diagnostics, such as morphology, Sérsic index, and kinematics should be combined when possible.

3.2 Intrinsic shapes

Different bulge formation mechanisms are thought to contribute to shape bulges in different ways. Costantin et al. (2018a) stated that the intrinsic shape of bulges provides a complementary classification between classical and pseudo-bulges. Their results are based on a statistical method to derive bulge intrinsic shapes from the observed projected 2D shape of galaxies (Méndez-Abreu et al. 2008, 2010; Costantin et al. 2018b). Here we compare the results of our simulations with the conclusions drawn from these observations.

We quantify the intrinsic 3D shapes of bulges by computing the eigenvalues of their mass distribution inertia tensor, adopting the same approach as M2019. We compute the principal axes of the mass distributions in the whole bulge, considering the center of the mass distribution as the most bound DM particle. Fig. 3 shows the c/a versus b/a diagram used by Costantin et al. (2018b) to analyse correlations between the intrinsic shapes and properties of bulges. They defined different regimes in this diagram, which are colour coded and indicated with text in Fig. 3. Auriga bulges occupy two well-defined loci. 53 per cent of the Auriga bulges show a very clear prolate shape, while the remaining 47 per cent are clustered in the region defined as the spherical regime. We find that the two major axes of the inertia tensor are well aligned, or have very low inclinations, with respect to the disc plane. Galaxies with bulges in the prolate regime are barred and the major axis of the mass tensor of bulges is in the direction of the bar major axis. We checked if excluding the stellar particles with $\epsilon > 0.7$ (see Section 2.2) has a significant effect on the shape of bulges. Oblate bulges, as currently defined, are still not present when considering all stellar particles inside 1 r_{eff}.

In the right-hand panels, we show the same diagram, but with symbols colour coded according to the Sérsic index (top) and B/T_{sim} ratio (bottom). We can see that bulges with higher Sérsic indexes tend to cluster in the spherical regime, with values of $0.8 \lesssim c/a \lesssim 0.9$ and $0.9 \lesssim b/a \lesssim 1$. Two bulges exhibit values of $b/a \approx 1$. The bulges with moderately high Sérsic indexes present more spherical shapes, as found by Costantin et al. (2018b). Bulges with lower Sérsic indexes tend to show more prolate shapes, although a group of them also occupies the spherical regime. This is in disagreement with the results of Costantin et al. (2018b), since they find that the low Sérsic index bulges are more commonly triaxial. Interestingly, none of our bulges show triaxial shapes. In the right bottom panel we see that bulges with larger values of B/T_v are also prone to occupy the prolate regime. This is at odds with the results shown by Costantin et al. (2018b), who found that bulges with larger B/T_v tend to be oblate systems. One possible reason for this discrepancy is that they probe the full range of disc morphologies, ranging from lenticulars to late-type spiral galaxies. Here we are narrowing the analysis to disc galaxies in MW-sized haloes, which are expected to have similarities in their formation mechanisms, unlike the broad sample selected in the CALIFA survey. This discrepancy can also arise because Costantin et al. (2018b) define a priori the orientation of the axes in the plane of the observed projected bulge, while we define the major, intermediate, and minor axes according to the mass distribution. A detailed analysis of the projected and intrinsic shapes of the bulges in high-resolution simulations with a broader range of DM haloes masses would be of great interest to constrain the connection between bulge shapes and their formation processes, and to shed light on this apparent discrepancy.

3.3 Degree of ordered rotation

The degree of ordered rotation of bulges is a fundamental quantity to discriminate between bulges and pseudo-bulges. The seminal work by Kormendy & Illingworth (1982) showed that bulges present kinematical properties that differentiate them from elliptical galaxies. They used the V_{max}/σ diagram (Illingworth 1977), where V_{max} is the maximum velocity in the line of sight (LOS), typically estimated using long-slit spectroscopy along directions parallel to the galaxy major axis, and σ is the velocity dispersion in the LOS. Classical bulges usually have some degree of ordered rotation and oblate shapes, while elliptical galaxies are supported by velocity dispersion and show anisotropy. When classical bulges coexist in barred disc galaxies, for example, they can acquire angular momentum from the bar (Saha 2015). For its part, pseudo-bulges usually show a higher degree of ordered rotation (Kormendy 1993; Kormendy & Kennicutt 2004) as their formation is linked to the discs and bars.

With the advent of integral-field spectroscopy surveys like SAURON (de Zeeuw et al. 2002), ATLAS^{3D} (Cappellari et al. 2011), or MaNGA (Bundy 2015), detailed kinematical structure in galaxies can be analysed. In this context, Binney (2005) proposed another way for computing V/σ that could take into account all the available observed data. Cappellari et al. (2007) used this for the first time, applied to the SAURON survey. We follow also this implementation and compute V/σ as

$$\left(\frac{V}{\sigma}\right)^2_e \equiv \frac{\langle V^2 \rangle}{\langle \sigma^2 \rangle} = \frac{\sum_{n=1}^{N} F_n V_n^2}{\sum_{n=1}^{N} F_n \sigma_n^2}, \quad (1)$$

where the index n denotes the nth-pixel of 0.2 squared kpc size in the edge-on view of Auriga galaxies inside one effective radius, a typical radial extent probed in the observations. For this calculation

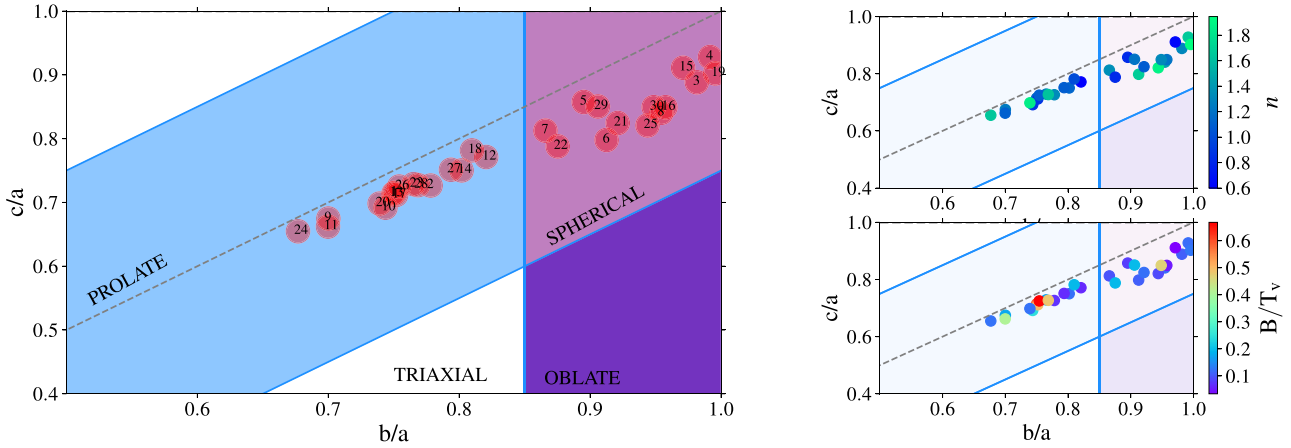

Figure 3. *Left-hand panel:* Intrinsic axial ratios c/a versus b/a for the Auriga bulges. The shaded areas in violet, pink, and light blue represent the oblate, spherical, and prolate regimes, respectively, defined in Costantin et al. (2018b). *Right-hand panels:* The same diagram as in the left-hand panel, but with bulges coloured by Sérsic index (top) and bulge-to-total ratio (bottom).

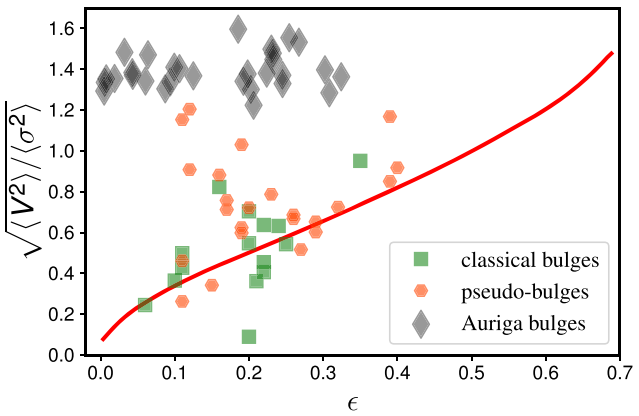

Figure 4. *Left-hand panel:* (V/σ, ϵ) diagram for our sample of Auriga bulges shown in black diamonds. Red hexagons and green squares are observational data from Fabricius et al. (2012). The red line indicates the oblate line that describes oblate spheroids that are isotropic and flattened only by rotation.

all stellar particles within one effective radius, including the disc, are taken into account, as done in observations. V_n and and σ_n are the mean velocity in the direction perpendicular to the x–z plane and the velocity dispersion, respectively, on the nth-pixel. F_n is the corresponding total flux. Ellipticity is obtained from the mass tensor analysis explained in Section 3.2 as

$$(1-\varepsilon)^2 = \frac{\langle y^2\rangle}{\langle x^2\rangle} = \frac{\sum_{n=1}^{N} F_n\, y_n^2}{\sum_{n=1}^{N} F_n\, x_n^2}, \quad (2)$$

where x and y are the main axes of the mass tensor of the region inside one effective radius.

In Fig. 4 we show the V/σ diagram for the Auriga bulges. They all show strong signatures of rotation in a moderate range of ellipticities. The oblate line is indicated with a red line. This line is approximated as $\epsilon/(1-\epsilon)^{1/2}$ and describes oblate spheroids that are isotropic and flattened only by rotation (Binney 1978; Kormendy & Illingworth 1982). Classical bulges in this diagram usually occupy positions near the oblate line or below and pseudo-bulges show usually a higher degree of ordered rotation. To illustrate this we also plot in Fig. 4 observational data from Fabricius et al. (2012). Auriga bulges show a higher degree of ordered rotation than the observed pseudo-bulges with a higher degree of ordered rotation found in Fabricius et al. (2012), reaching values of $V/\sigma > 1.5$. It is worth noting that we compute the LOS velocity with galaxies oriented perfectly edge-on. This is not the case for these observations, that were selected with inclinations low enough to classify bulges morphologically and velocities were later corrected for the inclination effect. The rotation degree shown by central regions of the Auriga simulations is a strong indication of the prevalence of pseudo-bulge formation in this sample of simulated galaxies.

4 FORMATION HISTORY OF THE AURIGA BULGES

In this section, we study the main physical mechanisms behind the formation of the bulges in the Auriga simulations. A fundamental step to understand the diversity in their formation history is to characterize the origin of the stellar particles that populate each of them.

4.1 Accreted versus in situ components

One possible and common practice to define their origin is to subdivide star particles according to whether they formed *in situ* or were accreted into the bulge from satellite galaxies (e.g. Zolotov et al. 2009; Tissera et al. 2012; Pillepich, Madau & Mayer 2015). Studies in the literature have subtle differences in these definitions and some grey areas can arise. For example, stars formed in a starburst during a merger event from gas coming from the satellite have been considered as both an accreted or *in situ* origin. Stars formed in tidal tails can cause the same ambiguity too.

Here, we define the accreted component of bulges as the stellar particles born bound to satellites of the host galaxy, that are members of the host bulge at $z = 0$ (see the definition of Auriga bulges in Section 2.2). On the other hand, the *in situ* component of the Auriga stellar bulges is defined as all $z = 0$ bulge stellar particles that were born inside the virial radius of the host galaxy and were not bound to any distinct satellite at the time of formation. This definition includes the star particles formed from the stripped gas accreted during a satellite accretion. In Fig. 5 we show the fractions of bulge

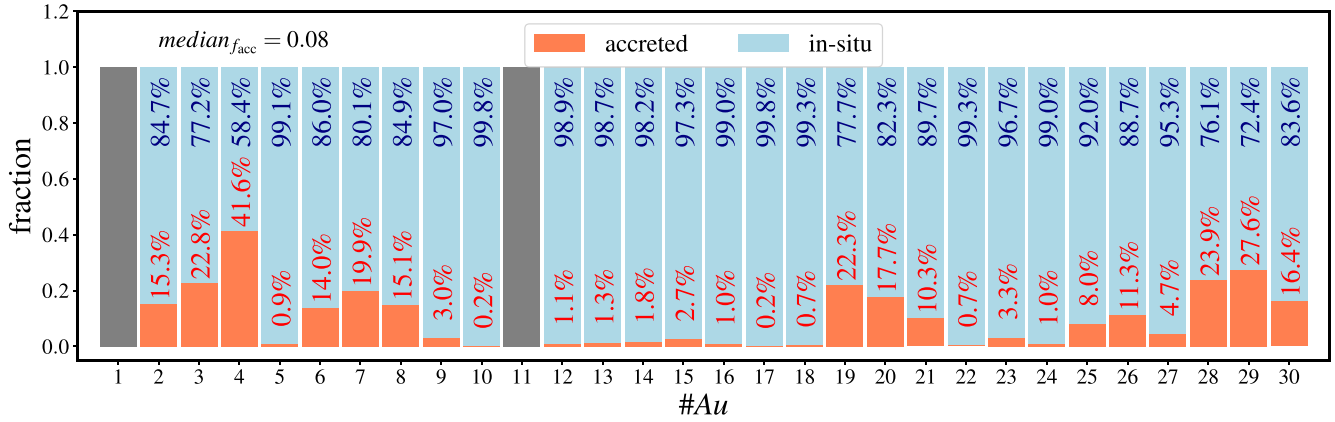

Figure 5. Fraction of accreted and *in situ* stars in bulges of the Auriga galaxies. Despite the rich merger history of the Auriga galaxies, all its bulges are dominated by *in situ* formed stars. The median accreted fraction is $f_{acc} = 0.08$. Moreover, 23 per cent of the simulated galactic bulges show negligible contributions from an accreted component. As indicated in the text Au 1 and Au 11 are excluded from this analysis because of ongoing merger activity.

stars that belong to the accreted and *in situ* components. Inside the bars, we show the fractions in terms ofpercentages. Au1 and Au11 bars are grey, because we exclude them from the current analysis. The reason for this is that both Au1 and Au11 show an ongoing major accretion event, which makes it difficult to define the different components of these galaxies. Only Au4 shows a considerable accreted bulge fraction of 0.42. In all the other cases, the accreted fractions are below 0.28 and for a few bulges like Au5, Au10, Au17, Au18, and Au22, the percentage of accreted material is less than 1 per cent. Despite the rich merger histories of many of our simulated galaxies (see e.g. M2019), the bulge accreted fractions are generally marginal.

In the left-hand and middle panels of Fig. 6 we show the mass density maps of the *in situ* and accreted bulge components of a subsample of Auriga bulges as seen edge-on and face-on, respectively. In the right-hand panels, we show the mass density profiles of both components, normalized to their corresponding maximum value. We choose three examples that depict three different types of behaviour of the accreted and *in situ* bulge components. We find that the *in situ* components are more centrally concentrated than the accreted counterparts in 14 bulges (∼50 per cent), as shown for Au3 in the first panel. The second panels show the example of Au6. Here the normalized spherical density distribution of the bulge accreted component follows almost exactly the one shown by *in situ* bulge. Simulated bulges that show this behaviour (∼11 per cent of Auriga bulges) have coincidentally a high fraction of accreted bulge stars. The similarity in the shape of the distribution could be the consequence of the violent relaxation of the stellar particles formed *in situ*, together with the accreted particles of a massive satellite. Indeed, the morphology of both components of Au6 shows a striking similarity in the left panels. Interestingly, for 4 out of 28 bulges (∼14 per cent) the accreted component follows the disc-like shape of their *in situ* component when seen edge-on (see Gómez et al. 2017a for a dedicated paper regarding the *ex situ* discs in the Auriga simulations), and the bar signature when seen face-on. The case of Au2 shown in the third panel is the clearest example where a bar-like distribution is seen in the accreted component. The remaining bulges (∼25 per cent of Auriga bulges) have too low accreted fractions to make a meaningful comparison between the spatial distribution of both components, but we note that in all these cases of low accreted bulge mass fractions, the accreted bulge components are also less concentrated than the *in situ* components. This result indicates that it is possible for the accreted stellar particle distribution to be reshaped by internal secular processes after being accreted (e.g. Saha, Martinez-Valpuesta & Gerhard 2012). The existence of this phenomenon in real galaxies could help to explain to some extent the apparent underabundance of classical bulges in disc galaxies.

4.2 Formation history of the *in situ* component

The simplest question that we can ask about the *in situ* population is where and when did it form. We show in Figs 7 and 8 the stellar particles formation time (age) distribution, t_{form}, of the $z = 0$ *in situ* bulge, as a function of birth radius, r_{birth}. Here r_{birth} is defined as the galactocentric distance of each particle at the nearest snapshot of their formation. In the Auriga simulations, the maximum spacing between snapshots is 203 Myr and the mean spacing is approximately 100 Myr. The blue dashed line on each panel represents the spatial extent of the bulge region. The percentages of stars formed inside and outside this limit are shown next to left and right of this line, respectively. In all cases, the birth radii distributions show that the star formation is peaked towards the central regions of the galaxy. This is in line with observations using the ALMA telescope that show high levels of star formation in the central regions of disc galaxies at high redshift ($z \sim 2$) (Tadaki et al. 2017). We can see that, although star particles are formed predominantly inside the bulge regions defined at $z = 0$, there are several galaxies which formed a large fraction of their *in situ* bulge outside this region. It is interesting to note the cases of Au10, Au12, Au13, Au15, Au17, Au18, Au22, Au26, and Au 28 which have an extended distribution and a dominant fraction ($f_{r_{birth}}^{>2reff} > 0.50$) of bulge stars that were formed outside the bulge region.

The bulge formation time distributions on the right axis of Figs 7 and 8 show great diversity and, in many cases, a high fraction of intermediate-age and young stars ($t_{form} < 8$ Gyr). The fraction of these younger stars in the *in situ* bulge, indicated for each simulation in Table 1, range from 0.11 for Au3 up to 0.94 for Au7. We can see star formation histories with peaks at different redshifts. During these peaks of star formation, the birth radii span a large range, sometimes reaching 10 kpc. Typically, these peaks are associated with mergers with satellite galaxies. The most relevant merger events are highlighted with arrows on each panel. The colours of the arrows indicate the total masses of the merging satellites, as indicated in the colour bar. We only show mergers with satellites

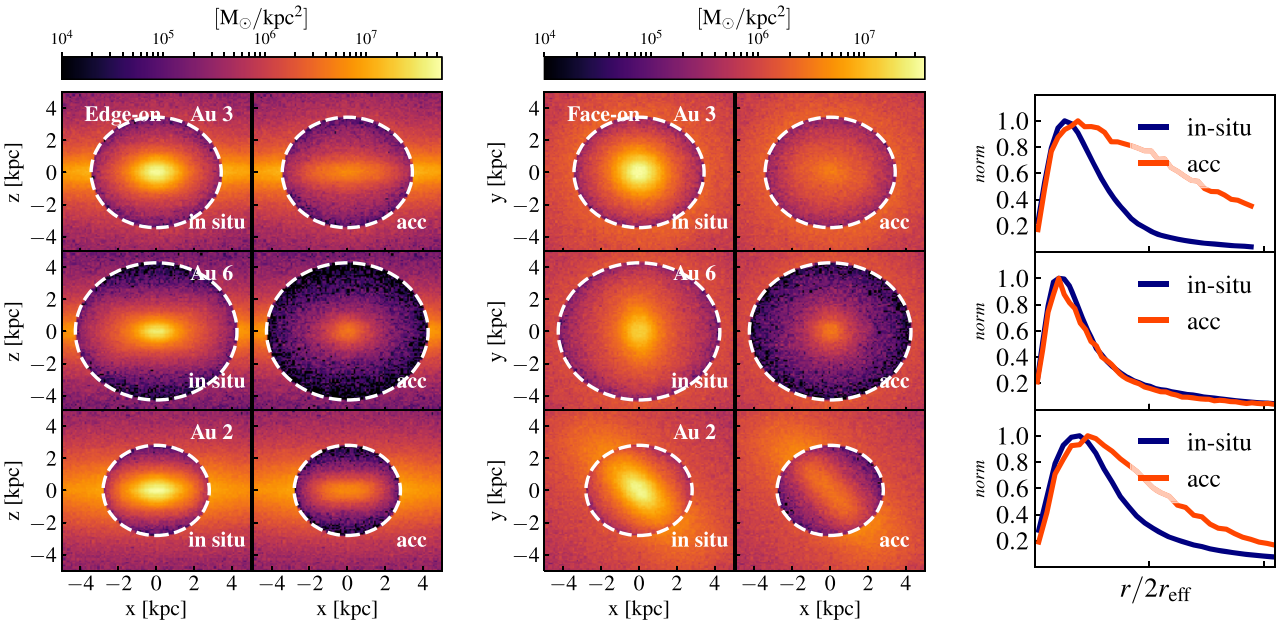

Figure 6. *Left-hand panels:* Projected density maps of the *in situ* and accreted components of bulges of a subsample of the Auriga galaxies as seen edge-on. The dashed white circle represents the bulge region within $2R_{\rm eff}$. *Middle panels*: Same as in left-hand panels, but as seen face-on. *Right-hand panels:* Normalized spherical density profiles of the *in situ* and accreted components as indicated in the legends. Au2 presents bar-shaped *in situ* and accreted components. Au3 shows an accreted component less concentrated than the *in situ* component. Au6 shows the same level of concentration in both components.

of total masses above $10^{10}\,{\rm M}_{\odot}$ that had occurred in the last 10 Gyr of the simulation. Interestingly, some of the peaks on the bulge star formation histories are associated with groups of small mergers instead of mergers with large satellites. However, not all peaks are correlated with galaxy mergers. For example Au17 shows several peaks of star formation with no associated merger. In many of those cases, we found that different forms of interactions due to flybys of massive satellites are triggering the star formation in the host galaxy (see e.g. Gómez et al. 2016a). During the mergers, the host discs are strongly perturbed and star formation is enhanced. Part of these newly formed stars settle down into the central regions as the system relaxes to an equilibrium. Additionally, a fraction of stars is formed in central starbursts driven by gas funneling in the case the merger is wet (Hopkins et al. 2009; Bustamante et al. 2018). Noticeably, the diversity shown in the star formation histories is shown to be related to the expected diverse merger histories experienced by the galaxies during their evolution in a cosmological scenario.

On the other hand, some of the simulations show extended star formation periods, which are associated with secular evolution processes within the galactic discs. The model Au18 provides a typical example of these processes. Au18 undergoes a merger with a satellite in the period between 8 and 9 Gyr ago, which is shown by the arrow and generates a strong $t_{\rm form}$ peak in Fig. 8. As shown by Grand et al. (2016a), who characterized the vertical heating of the Auriga discs as a function of time, Au18 develops a strong bar after this merger event (see their fig. 5). As a result, the star formation rate inside the bulge radius is increased by the funnelling of cold gas which loses angular momentum due to the torques exerted by the bar. Studies based on detailed hydrodynamic simulations have shown that the accretion of gas with low angular momentum in the inner galactic region produces off-axis shocks that drive gas into internal nuclear rings where stars are formed (Sanders & Huntley 1976; Kim et al. 2012, 2018). Other galaxies like Au17 and Au22 also show extended periods of star formation inside and outside the bulge region that are a consequence of secular evolution. These bulges develop strong non-axisymmetric instabilities during its evolution. In addition, direct cold gas accretion can also play a role in the enhancement of gas density and subsequent star formation both inside and outside the disc region (e.g. Sales et al. 2012). Au18 shows a significant fraction of bulge stellar particles that formed outside the bulge region after the merger event. These are particles that can be brought to the bulge due to an interplay of processes. It is well known that stars in discs can migrate from the original position where they were born in the galactic disc. Dynamical processes that are responsible for such behaviour are the presence of transient spiral arms, which change the angular momentum of stellar particles near the corotation radius and drive outward and inward streaming motions of these particles, and the resonant coupling between the bars and the spiral patterns (Sellwood & Binney 2002; Minchev & Famaey 2010; Grand, Kawata & Cropper 2012; Grand et al. 2016b). The same physical process can occur due to a bar, that can exert the loss of angular momentum to the particles captured in resonances. This way, particles can be caught inside the bulge radius during their orbit in the last snapshot of the simulation. Quantifying the evolution of bulges and the precise relative contributions of each mechanism is beyond the scope of this paper and is postponed to future work. The relative importance of these mechanisms of *in situ* bulge growth give place to the scatter that is seen in the Auriga bulges properties, together with the different accretion histories.

4.3 Accreted component: the bulge-stellar halo connection

In this section, we analyse the accreted component of the Auriga bulges, and its connection to the more extended stellar halo. As previously discussed in Section 4.1, the accreted component in all our models is subdominant, with a fractional mass that never surpasses the $f_{\rm acc} \lesssim 0.42$ and a median of $f_{\rm acc} = 0.08$. In Fig. 9 we dissect the total accreted bulge mass into different satellite

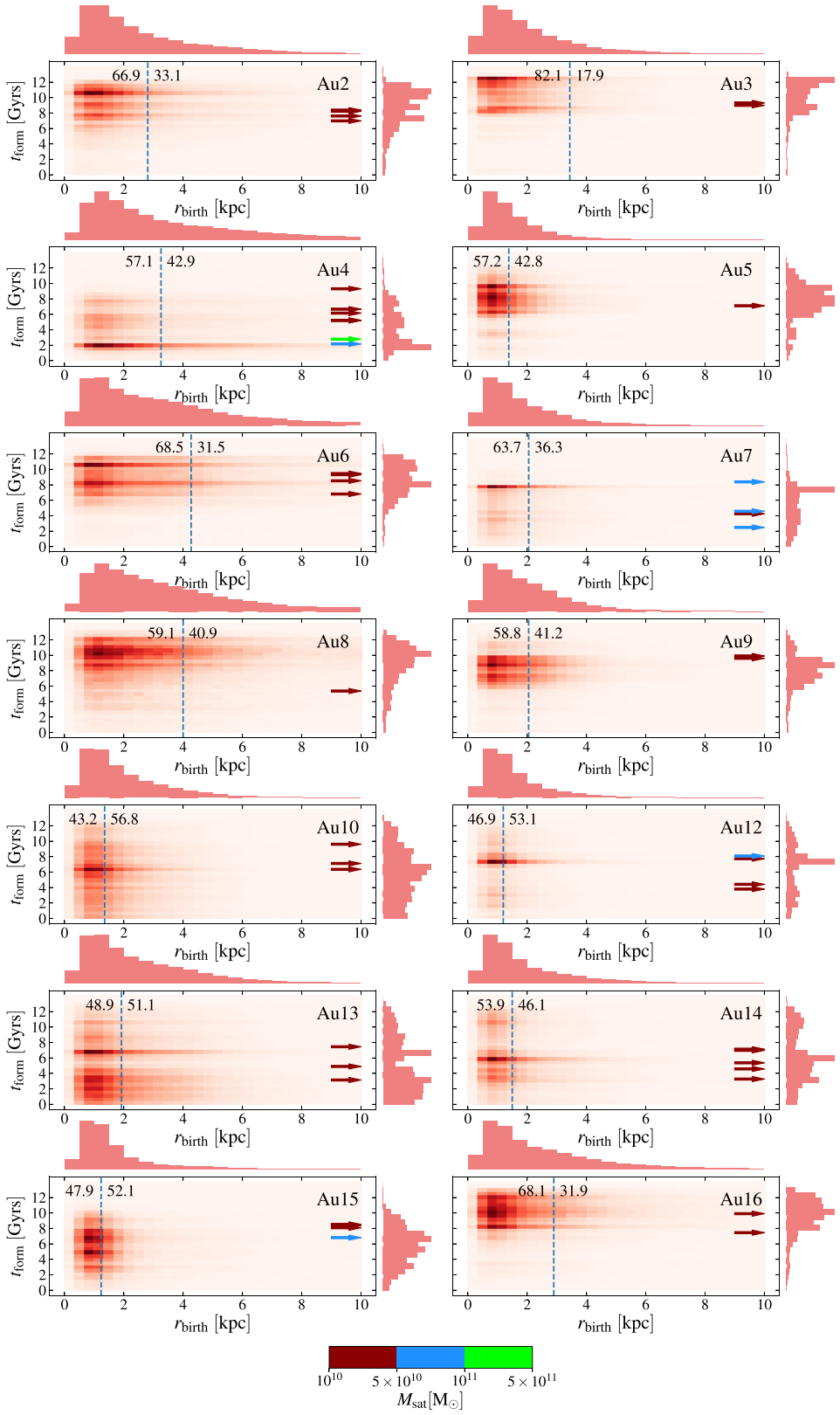

Figure 7. Formation times as a function of birth radii of stellar particles inside the bulge region at $z = 0$, for each of the first 14 Auriga simulations. Normalized distributions of birth radii and formation times are shown above the horizontal axis and to the right of the vertical axis, respectively. The vertical blue dashed lines indicate the spatial limit of the bulges at $z = 0$. The values to the left and right of the dashed lines indicate the fraction of *in situ* bulge stars formed inside and outside the bulge region, respectively. Merger times are indicated by arrows that are coloured according to the total mass of the merged satellite, as indicated by the colour bar. Only mergers with satellites of total masses above 10^{10} $M_\odot$ that had occurred in the last 10 Gyr of the simulation are shown in this figure.

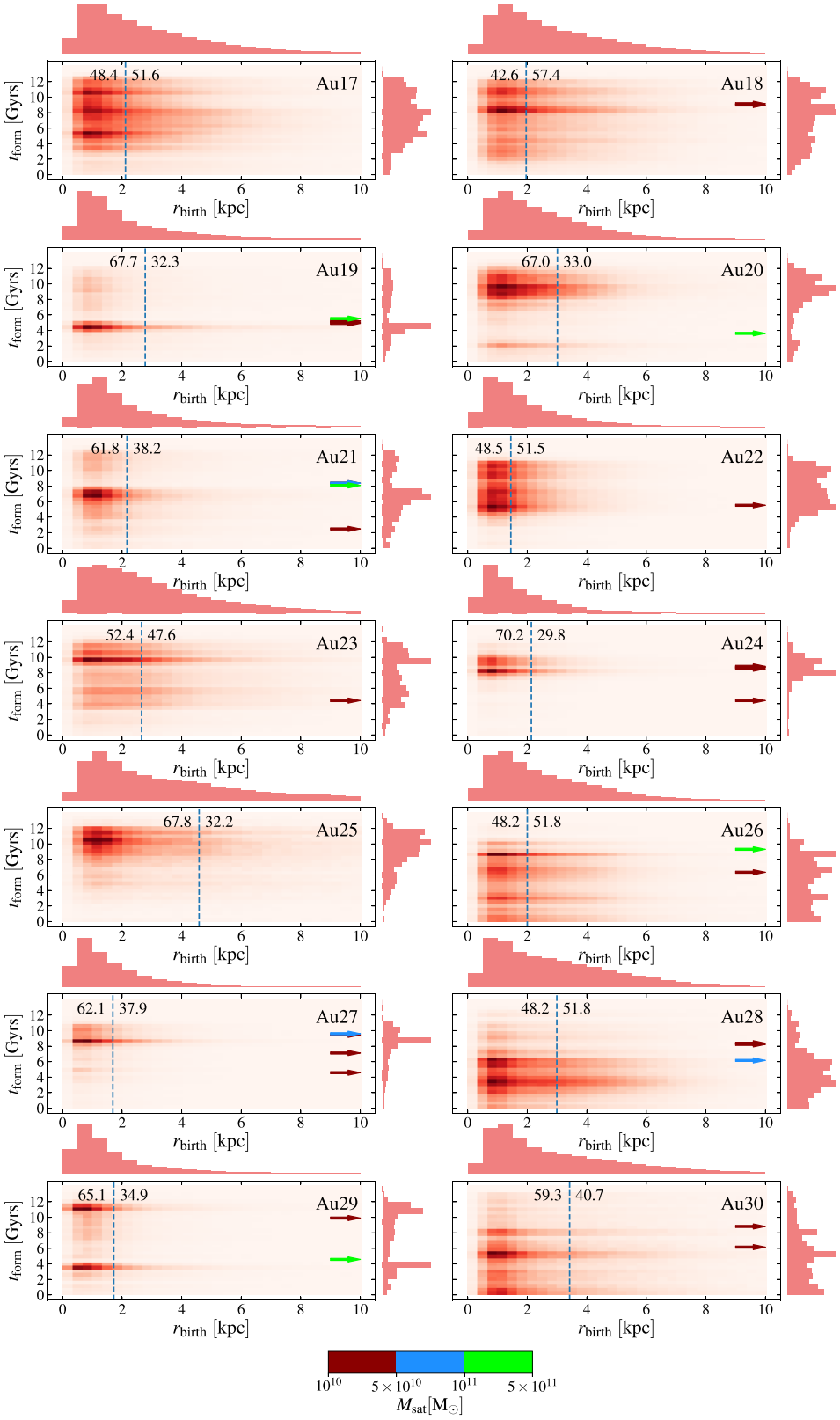

Figure 8. As in Fig. 7 for the rest of the 14 Auriga simulations.

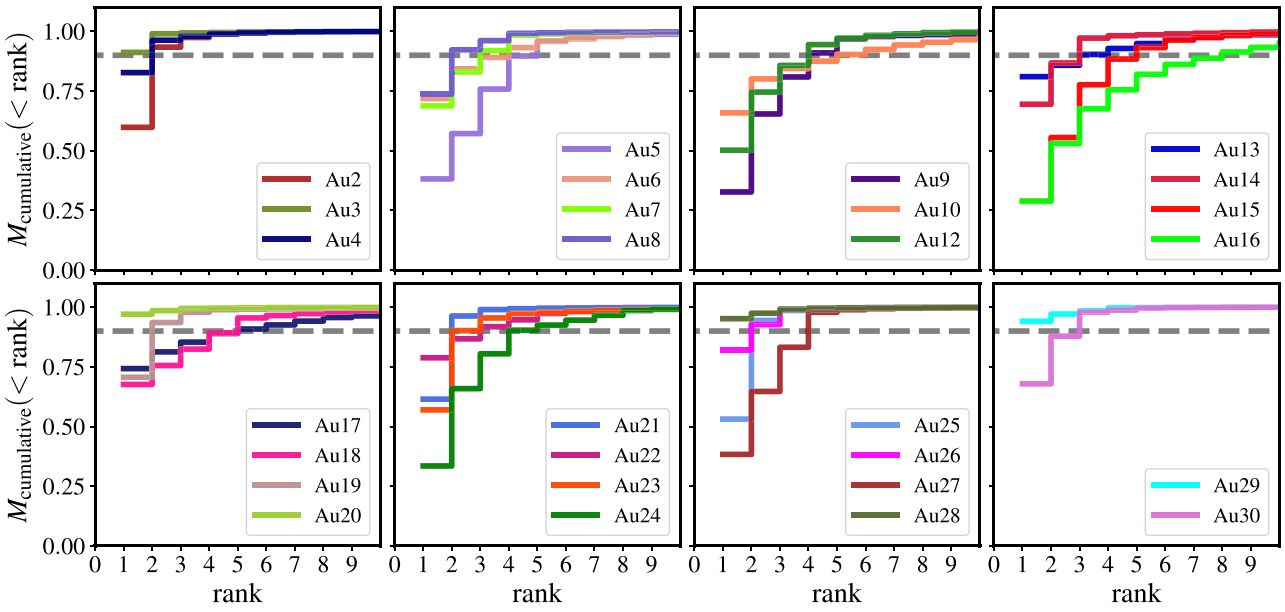

Figure 9. Cumulative accreted mass fraction from progenitors ranked by its contribution to the accreted component of the bulge. The higher rank (lower value) corresponds to the progenitor that contributed the most mass to the bulge. The grey dashed line represents the 90 per cent of the total accreted mass. Galaxies are presented in small groups in different panels for clarity.

contributors. Satellites are ranked according to their fractional mass contribution to the bulge in decreasing order (i.e. the larger the contributor, the smaller the rank assigned). We find that most of the accreted component (90 per cent) of each simulated bulge is formed from a low number of progenitors, between 1 for Au3 and 8 for Au16. Rather than from a continued assembly of mass coming from smooth accretion, we find that the accreted part of the Auriga bulges is mainly built-up from a few accretion events.

Now, we take a closer look at the progenitors of the accreted bulge component. In Fig. 10 we show, for the different progenitors, the contributed mass fraction to the accreted bulge against the total stellar mass associated with each progenitor. We only focus on satellites with stellar masses higher than $10^7\,{\rm M}_\odot$. In general, more massive progenitors contribute with more mass to the accreted bulge. However, we find several examples (1/3 of the Auriga bulges) in which the most massive progenitors have contributed with either negligible or small fractions to the accreted bulges. Examples are Au10, Au13, Au18, Au25, and Au30. This is typically the case for galaxies with negligible accreted bulge fractions ($f_{\rm acc,\,bulge} < 0.01$, see Fig. 5), for which we show the simulation identifier highlighted with a green rectangle in the corresponding panels. Most of the stellar mass brought in by these massive progenitors was either placed on the stellar halo (M2019) or in an *ex situ* disc component (Gómez et al. 2017b).

During the infall of a satellite galaxy, a fraction of their stars are stripped away by tidal forces and scattered to form the stellar halo (Searle & Zinn 1978; Helmi & White 1999; Bullock & Johnston 2005; Helmi 2008; Cooper et al. 2010). This places mergers as the main contributors to the formation of stellar haloes. Historically, mergers are considered to play an important role also in the formation of bulges (see Brooks & Christensen 2016, for a review), so following this scenario one should expect some relation between the growth of the stellar halo and the bulge of a given galaxy. The colour coding in Fig. 10 indicates the fraction of mass that each progenitor contribute to the total stellar halo at $z = 0$. M2019 already showed that also a few massive progenitors are responsible for the mass assembly of the majority of the stellar halo (> 90 per cent). Here we see that in many cases (see e.g. Au3, Au4, Au19, or Au20), some of the most significant progenitors of the stellar halo are also the most significant progenitors of the bulge. However, as previously stated, several counterexamples can be found.

Bell et al. (2017) compares the stellar masses of the bulges and haloes of nearby MW-mass galaxies (MW-peers); that is galaxies with stellar masses in the range of $3\text{–}12 \times 10^{10}\,{\rm M}_\odot$. The idea of this work was to study the relation between the formation of bulges and the merger history of galaxies. They found very little correlation between the accreted mass of the stellar haloes and the total mass of the bulges. To make a fair comparison with the observations, we computed the total bulge mass of the Auriga galaxies by multiplying the total stellar mass of the simulations by the bulge-to-total ratio obtained by integrating the fitted functions obtained in the two-component decomposition of surface brightness profiles (see Section 3) . This is how the total bulge mass was computed for the observed galaxies studied in Bell et al. (2017). The total stellar mass of each Auriga galaxy in this particular case was computed using the colour-dependent mass-to-light ratios from Bell et al. (2003). The $B - V$ colour and total luminosity in the K band were evaluated inside the optical radius of our simulations to derive the final total stellar mass. The resulting bulge stellar masses, for our models, computed following this procedure are shown in the left-hand panel of Fig. 11 as a function of the accreted stellar halo mass, obtained from M2019. In the right-hand panel we show the same relation as in the left-hand panel, but bulge stellar masses were computed as the sum of the stellar particle masses in the bulge as defined in Section 2.2. Our results in both panels reproduce qualitatively those obtained by Bell et al. (2017) for observed galaxies, also shown in Fig. 11 as grey symbols. There is no clear correlation between these two quantities in the Auriga galaxies. Although this is clear by eye, we computed the Pearson coefficient for the observations and the simulations, which measures the degree of linear correlation

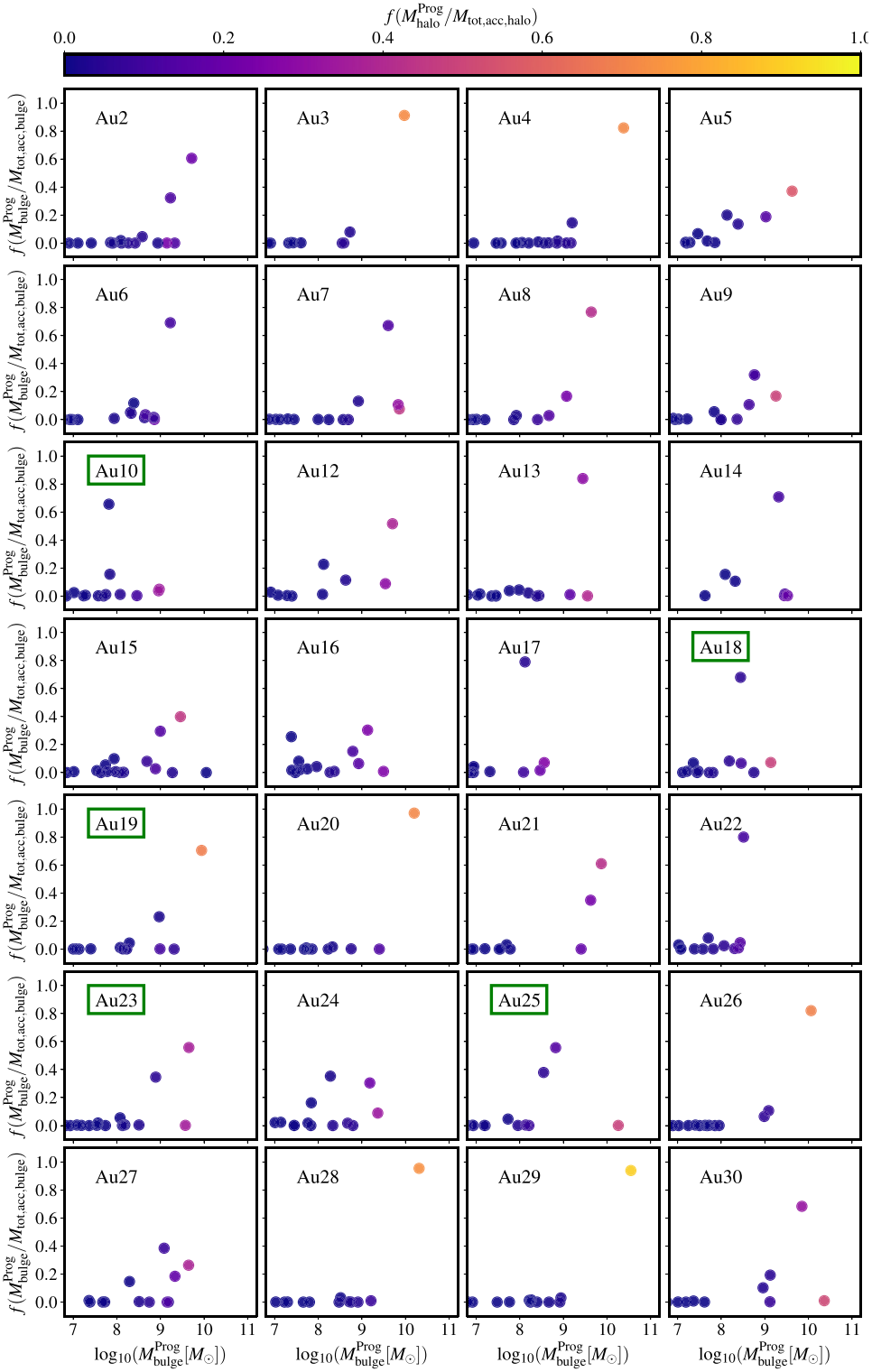

Figure 10. Fraction of mass that each progenitor (with stellar mass higher than 10^7 $M_\odot$) contributes to the bulge with respect to accreted bulge mass, as a function of the total stellar mass of the progenitor at the time of accretion into the host galaxy. The colouring of the points represents the fraction that each progenitor contributes to the stellar halo with respect to the total accreted mass in the halo. Green rectangles in the simulation identifier indicate the galaxies with accreted bulge fraction lower than 1 per cent.

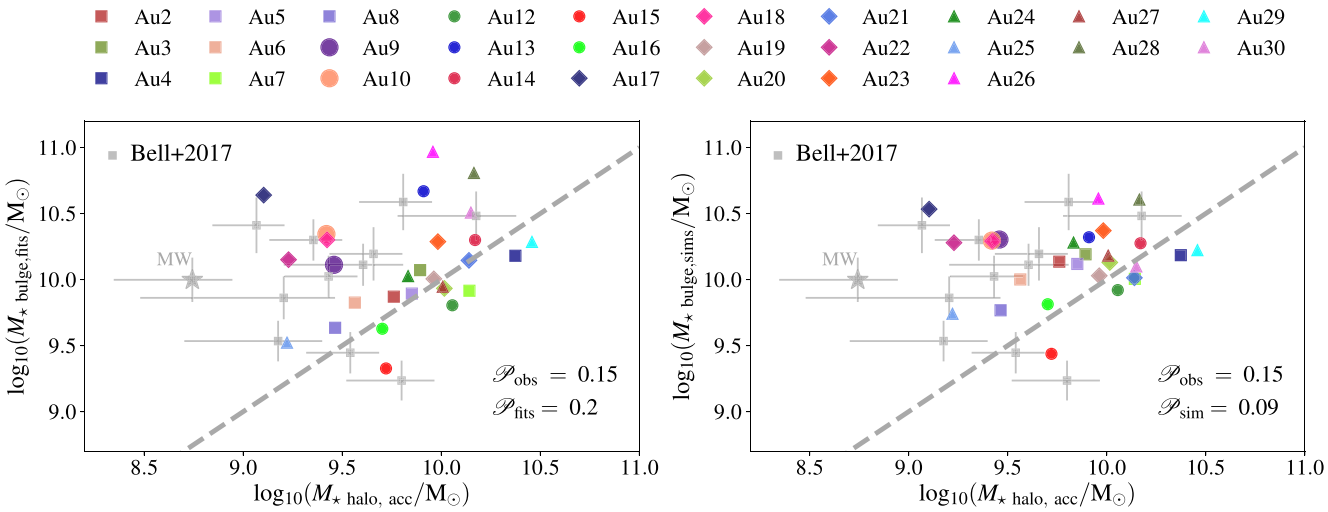

Figure 11. *Left-hand panel:* Stellar bulge mass as a function of accreted stellar halo mass. Bulge masses are estimated using the B/T_v ratio derived from surface brightness profiles as in the observations. Each colour indicates a galaxy, as labelled at the top. Grey points with errorbars are observed data from Bell et al. (2017). The grey dashed line indicates a 1:1 correlation for reference. No correlation in the Auriga bulges can be seen and little to no correlation can be seen in the observed sample. Pearson coefficients for the observed sample and simulated bulges are shown in the bottom right corner. Au 9, Au 10, Au17, Au22, and Au 26 show large bulge masses and low-mass-accreted stellar haloes. *Right-hand panel*: Same as in the left-hand panel, but bulge stellar masses are computed as the sum of the mass of stellar particles inside the bulge region defined in Section 2.2.

taking values between 1 and −1. The Pearson coefficient for the simulations in the right-hand panel is close to 0, indicating a null correlation. When using the luminosity-weighted bulge masses in the left panel the Pearson coefficient yields 0.2 and for the observed sample, the value is 0.15, larger, but still low. We find a group of galaxies (∼16 per cent of Auriga haloes) with low accreted stellar halo mass and a large bulge mass. This population is also present in the observed sample.

To further investigate the origin of the location of the Auriga galaxies in the bulge mass versus halo mass diagram, in the top panel of Fig. 12 we have colour-coded the symbols according to respective accreted bulge mass fraction. In this case we show the bulge masses computed directly from the simulation as in the right-hand panel of Fig. 11, since we cannot compute the accreted fractions of the bulge masses derived from the surface brightness profiles. Interestingly, the five simulations with a high bulge mass and low accreted halo mass (Au9, Au10, Au17, Au18, and Au22 in Fig. 11) all have negligible accreted bulge fractions. This fact alone, however, does not explain the offset from the broad relation followed by the other galaxies, since there are other galaxies with low accreted bulge fractions which do follow the weak trend between total bulge mass and accreted stellar halo mass (as we can see in Fig. 12). However, it is important to notice that these are some of the galaxies with the most massive bulges in our set of simulations.

As previously discussed in Section 4.2, Grand et al. (2016a) recently characterized the disc vertical heating of the Auriga galaxies, associated with non-axisymmetric disc perturbations and merger events. If we concentrate on the group of bulges with high total bulge mass but negligible accreted bulge fraction, Au17 and Au18 show two of the strongest bars in the whole simulation sample, that are present nearly during the entire evolution of these galaxies (see their fig. 5). Au9 develops a strong bar from 6 Gyrs ago until the present-day. Similar results are found for Au10 and Au22. High total bulge mass and low accreted bulge fraction is also seen in Au13, Au14 and Au23. However, they do follow the broad M_{bulge} versus M_{halo}^{acc} correlation in the diagram more

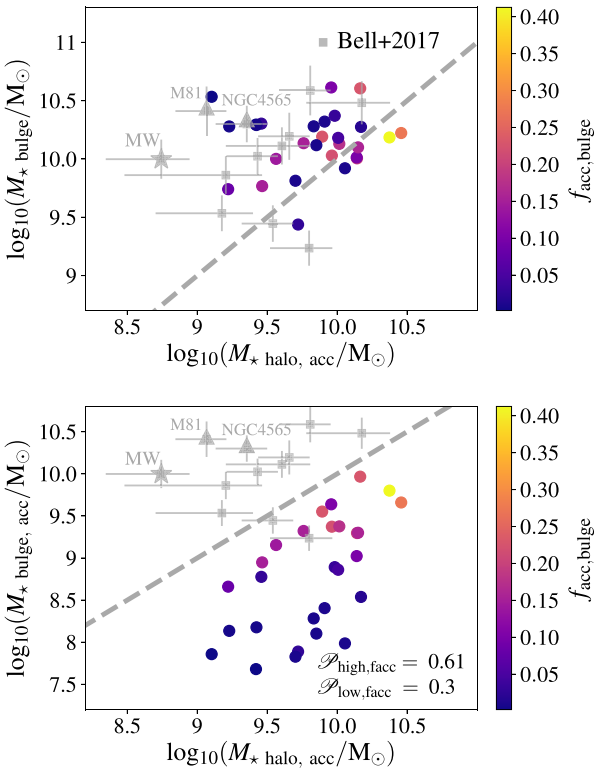

Figure 12. Total bulge stellar mass (top) and accreted bulge stellar mass (bottom) as a function of accreted stellar halo mass. Points are coloured according to the accreted fraction of stars of each bulge. Grey points with errorbars are observed data from Bell et al. (2017) and the grey dashed line indicates a 1:1 correlation for reference. The group of high total bulge mass, mentioned in Fig. 11, presents marginal accreted bulge fractions. Galaxies with higher accreted bulge fractions show a tight correlation in the bottom panel. Pearson coefficients are shown for galaxies with high and low accreted bulge fraction ($f_{acc,bulge} > 0.05$ and $f_{acc,bulge} < 0.05$), respectively.

closely, mainly thanks to their larger $M_{\rm halo}^{\rm acc}$ mass. We find that these galaxies develop relatively strong non-axisymmetric disc features during their evolution. In addition, they experienced a relatively massive merger, which contributed to the formation of the *in situ* bulge through the triggering of central star formation bursts and tidal perturbation of the pre-existing discs (see Figs 7 and 8), but mainly increasing the accreted halo mass, $M_{\rm halo}^{\rm acc}$. This can be seen in Fig 10.

Based on our results, one can infer that galaxies with low accreted stellar halo and high total bulge mass (Au9, Au10, Au17, Au18, and Au22) have a low bulge accreted mass fraction, and that non-axisymmetric disc perturbations have played a significant role in the build-up of the total bulge mass. Following this, M81 and NGC 4565, highlighted in Fig. 12 with grey triangles, should have a low fractional contribution of an accreted bulge component with respect to the *in situ* bulge component and that, probably, they have developed strong non-axisymmetric features, such as bars or transient spiral arms, sometime during their evolution. NGC 4565 was studied recently by Kormendy & Bender (2019) and indeed fit this scenario showing lack of a classical bulge component and the presence of an X-shape central region attributed to a bar. M81, for its part, does not show a visible bar, but it is known for its strong spiral pattern (Kendall et al. 2008). Considering our findings, a possible scenario for the apparent excessive mass of M81's bulge in relation with its stellar halo mass is that an ancient bar might have developed sometime in this galaxy.

In the bottom panel of Fig. 12 we show the accreted bulge mass as a function of the accreted stellar halo mass, colour-coded by the accreted bulge fraction. We can see that the accreted bulge mass correlates with the accreted halo mass. Bulges with high accreted fraction show a tight correlation, close to a 1:1 correlation, whilst bulges with low and negligible accreted fractions show a larger scatter. In order to quantify the difference, we computed the pearson coefficients obtained for galaxies with accreted bulge fractions $f_{\rm acc} > 0.05$ and for those with lower accreted bulge fractions separately. The high accreted bulge fraction group shows a pearson coefficient of 0.76 and the group with low accreted bulge fraction has a pearson coeficcient of 0.42, as indicated in the bottom right corner of the bottom panel.

5 DISCUSSION

Historically, simulations of galaxy formation within a ΛCDM framework suffered the overcooling problem (Balogh et al. 2001). Simulations produced highly concentrated galaxies with bulges that exceeded the observed sizes and bulge-to-total ratios (Christensen et al. 2014). With the implementation of plausible sub-grid physics in hydrodynamical simulations that take into account energetic feedback processes, the excess of concentrated star formation was suppressed (Springel & Hernquist 2003; Ceverino & Klypin 2009), although, sometimes, at the expense of destroying the morphology of the galactic discs (Roškar et al. 2014). In the case of the Auriga galaxies, the stellar feedback produces a moderate thickening of the discs but preserves properties that reproduce several observational trends (G2017). With regard to the bulges, we found that the Auriga galaxies show a systematic excess in the effective radii related to an excess in the total mass of bulges. Because of this excess, 23 per cent of Auriga bulges have surface brightness inside effective radius and total magnitude with no counterpart in nature. This excess could be related to the implementation of the stellar feedback in the Auriga simulations, which has been shown to produce a milder effect than expected in the quenching of dwarf galaxies (Simpson et al. 2018).

One of the main results of this paper is the predominant *in situ* formation of the Auriga bulges. In a recent work, Gargiulo et al. (2017) studied the stellar populations of galactic bulges in MW-like galaxies using a semi-analytic model of galaxy formation (Gargiulo et al. 2015; Cora et al. 2018), coupled to cosmological *N*-body simulations, and found that on average approximately 16 per cent of the bulge mass has an accreted origin. Other cosmological simulations show similar results. Tissera et al. (2018) show the fraction of accreted mass as a function of galactocentric distances in their fig. 2, and even though the inner spheroid includes some transitional region to the stellar halo, we can see that the accreted fractions inside 4 kpc are also between 0.02 and 0.15. Guedes et al. (2013) reports an accreted fraction of only 4 per cent in the pseudo-bulge of an MW-like galaxy simulation. Buck et al. (2019) found a contribution of 2.3 per cent of accreted stars to the bulge components. Wang et al. (2019) analysed a set of ten galaxies of the NIHAO project (Wang et al. 2015) and found that, on average, 95 per cent of stars in bulges have an *in situ* origin. Ours and previous results suggest that bulges of simulated disc galaxies formed in MW-sized DM haloes in a cosmological context commonly lack a strong accreted component.

When we look exclusively at the accreted stellar particles that are part of bulges at $z = 0$ we found that a low number of satellite galaxies (the most massive progenitors in the history of accretion in general) are responsible for the build-up of the accreted bulge component of galaxies (see Figs 9 and 10). This result suggests that many mergers with very small satellites are not centrally responsible for the growth of galactic bulges. A similar result was found for the stellar haloes of the Auriga simulations by M2019. As also noted by M2019, this is in line, for example, with the formation scenario of the stellar halo of M31, for which a single satellite is found to account for the build-up of most of its stellar halo (see also D'Souza & Bell 2018a,b). Following our findings, this single satellite could also be responsible for most of the accreted component of its bulge. Although one might at first think that a halo or accreted component of a bulge built from one or a few progenitors would have relatively homogeneous populations, in fact, the haloes built from few massive progenitors have complex star formation histories and gradients inherited from the massive satellite that it accreted (D'Souza & Bell 2018a,b).

Mergers are a natural outcome of the lambda cold dark matter (ΛCDM) scenario, in which DM haloes, where galaxies are formed, growth hierarchically from smaller structures. Theoretical predictions of merger rates are in close agreement with estimates of merger rates using pair fractions. Mundy et al. (2017) used this method to estimate observational merger rates and compared with results using the ILLUSTRIS simulation (Rodriguez-Gomez et al. 2017), and merger rates derived from light cones derived from a semi-analytic model (Henriques et al. 2015), and found a good agreement. The influence of mergers in the formation of bulges is found to be central in many simulations. Major mergers are common at high redshift, but after $z \sim 1$ become rare for galaxies with masses in the range of the MW-mass. Garrison-Kimmel et al. (2018) show using the LATTE simulations (Wetzel et al. 2016), that most of the stars in their simulations are born with disc-like kinematics and that gas-rich mergers are one of the main drivers of bulge formation at high redshift.

It is often claimed that the hierarchical paradigm is in tension with the lack of classical bulges in bright disc galaxies like the MW (see for example Kormendy et al. 2010; Shen et al. 2010; Kormendy 2016). It is important to highlight the fact that most large disc galaxies in the local Universe have pseudo-bulges is not

at odds with galaxy formation in a hierarchical context, as can be seen in the results of our study. Results presented in this work show that mergers funnel gas into the central parts of the galaxy forming bulges that do not necessarily show a dominant dispersion-dominated component that resembles a mini-elliptical galaxy at present, as indicated by the properties of the surface brightness profile at $z = 0$, such as the Sérsic index (see Table 1), its shape (see Fig. 3), and the degree of ordered rotation (see Fig. 4). Even though most of the Auriga simulations present rich merger histories and some of the simulated bulges have large accreted fractions (for example Au4), we found, applying criteria based on those used in observations that the majority of bulges in our sample can be classified as pseudo-bulges.

Bulges formed by mergers can change their shape during their evolution. It is possible that the formation of a bar on top of a small classical bulge formed at high redshift can dynamically affect the non-rotating component, making it indistinguishable from a pseudo-bulge at $z = 0$, as is demonstrated by simulations (Saha et al. 2012; Saha 2015) and as can be seen clearly in the case of Au2 in Fig. 6. Moreover, mergers or interactions with satellite galaxies can play an important role in the formation of pseudo-bulges, by instigating the formation of bars in globally unstable systems (Byrd et al. 1986; Noguchi 1987; Romano-Díaz et al. 2008). We see this occurring in some Auriga galaxies, see e.g. the case of the formation of the bulge in Au18 which was discussed in Section 4.2. In that case, a strong bar is developed after a major merger. Because of this, we stress that studying the formation of the innermost regions of galaxies, where bulges arise, without a hydrodynamical cosmological framework could lead to oversimplified scenarios of the bulge formation in the cases when the accreted component of the galaxy is significant.

As stated before in Section 2, the question of environment could play a role here. Although the accretion histories were not explicitly constrained, and a good diversity of accretion histories is available, the Auriga simulations were run adopting an isolation criterion for the host DM haloes. MW-analogues in denser environments might suffer later and more numerous accretion events on average and, therefore, contain central regions with a higher degree of random motions. Bars can be destroyed by these interactions, limiting important channels of mass formation via secular processes described in Section 4.2.

6 SUMMARY AND CONCLUSSIONS

We have analysed the properties and the origin of galactic bulges in 30 cosmological magneto-hydrodynamical simulations of disc galaxies in MW-sized DM haloes. The Auriga simulations have a baryonic resolution of $\sim 5 \times 10^4\,\mathrm{M}_\odot$, and represent one of the largest samples of cosmological collisional simulations at this level of resolution to date. We found a great diversity of bulges in a narrow range of DM halo masses. This diversity is similar to that observed and should be regarded as a good asset to learn about the formation history of the MW and MW-analogues, such as M31, NGC 4565, and NGC 5746 (Bell et al. 2017; Kormendy & Bender 2019). We list here our main results.

(i) Galactic bulges in the Auriga simulations have considerable diversity in general properties such as morphology, surface brightness, and shape. However, compared with the sample of disc galaxies in the local Universe of Fisher & Drory (2008), the Auriga bulges occupy a rather narrow range in size in the Kormendy diagram. They show a systematic excess in effective radii compared with the observed sample at high surface brightness.

(ii) All bulges in the Auriga galaxies have properties that would define them photometrically as pseudo-bulges. Sérsic indices derived from surface brightness profiles are found to be all $n < 2$ and their behaviour in the $M_v - \mu_e$ diagrams is closer to that observed for pseudo-bulges. Although, 23 per cent of bulges have higher surface brightness than any observed bulge and are more luminous than observed pseudo-bulges.

(iii) Auriga bulges occupy two marked loci in a diagram that relates the axial ratios of their mass distributions. One group shows marked prolate intrinsic shapes due to the presence of a bar, while the other has close to spherical mass distributions. We found that the more nearly to spherical group has lower $\mathrm{B/T_{sim}}$ ratios and higher Sérsic indices. Prolate bulges develop in barred galaxies and are in general more massive and have lower Sérsic indices.

(iv) Auriga bulges show a high degree of ordered rotation and low ellipticities in the $(V/\sigma)-\epsilon$ diagram, well above the region occupied by observed classical bulges.

(v) Auriga bulges are formed predominantly *in situ* (see Fig. 5). The largest accreted bulge fraction reaches $f_{\mathrm{acc}} = 0.42$, and only 21 per cent of bulges have accreted fractions higher than $f_{\mathrm{acc}} = 0.2$. 21 per cent of bulges have negligible accreted fractions (less than $f_{\mathrm{acc}} = 0.01$).

(vi) The spatial distributions of the accreted and *in situ* bulge components show different behaviours. 50 per cent of the Auriga bulges possess a less concentrated accreted component compared to the *in situ* component, whereas 11 per cent of bulges show that these components have a similar normalized spherical density distribution. Interestingly, 14 per cent of bulges show accreted components that follow the shape of the bar seen in the corresponding *in situ* components. The remaining bulges have too low or negligible accreted fractions to make a meaningful comparison.

(vii) Analysis of the *in situ* component of bulges show that bulge stellar particles form predominantly in the central regions of the galaxy, although a low fraction of the sample show approximately equal parts formed outside and inside $2r_{\mathrm{eff}}$ at $z = 0$. Some of them that happen to develop a strong bar during the evolution form more stars outside the bulge radius than inside. This underscores the significance of secular evolution to the growth of bulges in these galaxies. Mergers are also responsible to the *in situ* star formation inside the bulge. *In situ* star formation histories of the Auriga bulges show peaks when a single or several minor mergers occur between snapshots. The strength of these peaks correlates broadly with the mass of the satellites. The star formation history of the *in situ* bulge component shows greater diversity, due to the contribution of different mechanisms to *in situ* bulge growth and the inherent diversity of merger histories.

(viii) The accreted components of bulges in the Auriga simulations are dominated by a single accretion in 80 per cent of the cases. Most of the remainder of the mass originates from the next few most massive accretions, which happen to be the more massive satellites that were accreted by the galaxies, in most cases. In addition, the same satellites typically contributed more to the build-up of the corresponding stellar halo. Accretion of stars by a large number of mergers with very small satellites is therefore not a favoured mechanism of the accreted bulge growth in MW-sized galaxies in our models. However, as mentioned before, minor mergers play an important role in the *in situ* star formation inside the bulge.

(ix) Total bulge mass and accreted stellar halo mass show little correlation as noted in observations. Those galaxies with a low accreted bulge fraction show no correlation between stellar halo mass and total bulge mass, but a group of them that develop strong bars during its evolution, occupy a well defined region in the bulge

mass versus accreted stellar halo mass diagram. This result can help to constrain the origin of bulge stars in observed galaxies according to the position in this diagram. Accreted bulge mass and accreted stellar halo mass are correlated. Galaxies with higher accreted bulge fraction show lower dispersion than galaxies with low accreted bulge fraction in this relation.

This is the first paper in a series studying the formation of bulges in MW-sized DM haloes. An even larger sample of high-resolution simulations spanning a broader range in DM halo masses is necessary to understand the transition in the formation of pseudo-bulges and classical bulges in disc galaxies.

ACKNOWLEDGEMENTS

We wish to thank David Campbell and Adrian Jenkins for generating the initial conditions and selecting the sample of the Auriga galaxies. IG acknowledges financial support from CONICYT Programa de Astronomía, Fondo ALMA-CONICYT 2017 31170048. AM acknowledges support from CONICYT FONDECYT Regular grant 1181797. FAG acknowledges support from CONICYT FONDECYT Regular grant 1181264. IG, AM, and FAG acknowledge funding from the Max Planck Society through a 'Partner Group' grant. FM acknowledges support through the program 'Rita Levi Montalcini' of the italian MIUR. This work used the DiRAC Data Centric system at Durham University, operated by the Institute for Computational Cosmology on behalf of the STFC DiRAC HPC Facility (www.dirac.ac.uk). This equipment was funded by BIS National E-infrastructure capital grant ST/K00042X/1, STFC capital grant ST/H008519/1, and STFC DiRAC Operations grant ST/K003267/1 and Durham University. DiRAC is part of the National E-Infrastructure.

REFERENCES

Abadi M. G., Navarro J. F., Steinmetz M., Eke V. R., 2003, ApJ, 591, 499
Balogh M. L., Pearce F. R., Bower R. G., Kay S. T., 2001, MNRAS, 326, 1228
Bell E. F., McIntosh D. H., Katz N., Weinberg M. D., 2003, ApJS, 149, 289
Bell E. F., Monachesi A., Harmsen B., de Jong R. S., Bailin J., Radburn-Smith D. J., D'Souza R., Holwerda B. W., 2017, ApJ, 837, L8
Binney J., 1978, MNRAS, 183, 501
Binney J., 2005, MNRAS, 363, 937
Brooks A., Christensen C., 2016, in Laurikainen E., Peletier R., Gadotti D., eds, Astrophysics and Space Science Library, Vol. 418, Galactic Bulges, Springer International Publishing, Switzerland, p. 317
Bruzual G., Charlot S., 2003, MNRAS, 344, 1000
Buck T., Ness M., Obreja A., Macciò A. V., Dutton A. A., 2019, ApJ, 874, 67
Buck T., Ness M. K., Macciò A. V., Obreja A., Dutton A. A., 2018, ApJ, 861, 88
Bullock J. S., Johnston K. V., 2005, ApJ, 635, 931
Bundy K. et al.., 2015, ApJ, 798, 7
Bustamante S., Sparre M., Springel V., Grand R. J. J., 2018, MNRAS, 479, 3381
Byrd G. G., Valtonen M. J., Sundelius B., Valtaoja L., 1986, A&A, 166, 75
Cappellari M. et al., 2007, MNRAS, 379, 418
Cappellari M. et al., 2011, MNRAS, 413, 813
Ceverino D., Klypin A., 2009, ApJ, 695, 292
Chabrier G., 2001, ApJ, 554, 1274
Christensen C. R., Brooks A. M., Fisher D. B., Governato F., McCleary J., Quinn T. R., Shen S., Wadsley J., 2014, MNRAS, 440, L51
Cooper A. P. et al., 2010, MNRAS, 406, 744
Cooper A. P., Parry O. H., Lowing B., Cole S., Frenk C., 2015, MNRAS, 454, 3185
Cora S. A. et al., 2018, MNRAS, 479, 2
Costantin L., Corsini E. M., Méndez-Abreu J., Morelli L., Dalla Bontà E., Pizzella A., 2018a, MNRAS, 481, 3623
Costantin L., Méndez-Abreu J., Corsini E. M., Eliche-Moral M. C., Tapia T., Morelli L., Dalla Bontà E., Pizzella A., 2018b, A&A, 609, A132
D'Souza R., Bell E. F., 2018a, Nat. Astron., 2, 737
D'Souza R., Bell E. F., 2018b, MNRAS, 474, 5300
de Zeeuw P. T. et al., 2002, MNRAS, 329, 513
Debattista V. P., Ness M., Gonzalez O. A., Freeman K., Zoccali M., Minniti D., 2017, MNRAS, 469, 1587
Debattista V. P., Gonzalez O. A., Sanderson R. E., El-Badry K., Garrison-Kimmel S., Wetzel A., Faucher-Giguère C.-A., Hopkins P. F., 2019, MNRAS, 485, 5073
Di Matteo P. et al., 2015, A&A, 577, A1
Fabricius M. H., Saglia R. P., Fisher D. B., Drory N., Bender R., Hopp U., 2012, ApJ, 754, 67
Faucher-Giguère C.-A., Lidz A., Zaldarriaga M., Hernquist L., 2009, ApJ, 703, 1416
Fisher D. B., Drory N., 2008, AJ, 136, 773
Fisher D. B., Drory N., 2011, ApJ, 733, L47
Fisher D. B., Drory N., 2016, in Laurikainen E., Peletier R., Gadotti D., eds, Astrophysics and Space Science Library, Vol. 418, Galactic Bulges, Springer International Publishing, Switzerland, p. 41
Fragkoudi F., Di Matteo P., Haywood M., Gómez A., Combes F., Katz D., Semelin B., 2017, A&A, 606, A47
Gadotti D. A., 2009, MNRAS, 393, 1531
Gargiulo I. D. et al., 2015, MNRAS, 446, 3820
Gargiulo I. D., Cora S. A., Vega-Martínez C. A., Gonzalez O. A., Zoccali M., González R., Ruiz A. N., Padilla N. D., 2017, MNRAS, 472, 4133
Garrison-Kimmel S. et al., 2018, MNRAS, 481, 4133
Gómez F. A., White S. D. M., Marinacci F., Slater C. T., Grand R. J. J., Springel V., Pakmor R., 2016a, MNRAS, 456, 2779
Gómez F. A., White S. D. M., Marinacci F., Slater C. T., Grand R. J. J., Springel V., Pakmor R., 2016b, MNRAS, 456, 2779
Gómez F. A., White S. D. M., Grand R. J. J., Marinacci F., Springel V., Pakmor R., 2017a, MNRAS, 465, 3446
Gómez F. A. et al., 2017b, MNRAS, 472, 3722
Gómez A., Di Matteo P., Schultheis M., Fragkoudi F., Haywood M., Combes F., 2018, A&A, 615, A100
Grand R. J. J., Kawata D., Cropper M., 2012, MNRAS, 421, 1529
Grand R. J. J., Springel V., Gómez F. A., Marinacci F., Pakmor R., Campbell D. J. R., Jenkins A., 2016a, MNRAS, 459, 199
Grand R. J. J. et al., 2016b, MNRAS, 460, L94
Grand R. J. J. et al., 2017, MNRAS, 467, 179
Guedes J., Callegari S., Madau P., Mayer L., 2011, ApJ, 742, 76
Guedes J., Mayer L., Carollo M., Madau P., 2013, ApJ, 772, 36
Harmsen B., Monachesi A., Bell E. F., de Jong R. S., Bailin J., Radburn-Smith D. J., Holwerda B. W., 2017, MNRAS, 466, 1491
Helmi A., 2008, A&AR, 15, 145
Helmi A., White S. D. M., 1999, MNRAS, 307, 495
Henriques B. M. B., White S. D. M., Thomas P. A., Angulo R., Guo Q., Lemson G., Springel V., Overzier R., 2015, MNRAS, 451, 2663
Hopkins P. F., Cox T. J., Younger J. D., Hernquist L., 2009, ApJ, 691, 1168
Illingworth G., 1977, ApJ, 218, L43
Kauffmann G., White S. D. M., Guiderdoni B., 1993, MNRAS, 264, 201
Kendall S., Kennicutt R. C., Clarke C., Thornley M. D., 2008, MNRAS, 387, 1007
Kim E., Kim S. S., Choi Y.-Y., Lee G.-H., de Grijs R., Lee M. G., Hwang H. S., 2018, MNRAS, 479, 562
Kim W.-T., Seo W.-Y., Stone J. M., Yoon D., Teuben P. J., 2012, ApJ, 747, 60
Kormendy J., 1977, ApJ, 218, 333
Kormendy J., 1993, in Dejonghe H., Habing H. J., eds, Proc. IAU Symp. 153, Galactic Bulges, Kluwert Academic Publishers, Dordrecht, p. 209
Kormendy J., 2016, in Laurikainen E., Peletier R., Gadotti D., eds, Astrophysics and Space Science Library, Vol. 418, Galactic Bulges, Springer International Publishing, Switzerland, p. 431
Kormendy J., Bender R., 2019, ApJ, 872, 106

Kormendy J., Illingworth G., 1982, ApJ, 256, 460
Kormendy J., Kennicutt Robert C. J., 2004, ARA&A, 42, 603
Kormendy J., Drory N., Bender R., Cornell M. E., 2010, ApJ, 723, 54
Marinacci F., Pakmor R., Springel V., 2014, MNRAS, 437, 1750
McWilliam A., Zoccali M., 2010, ApJ, 724, 1491
Méndez-Abreu J., Aguerri J. A. L., Corsini E. M., Simonneau E., 2008, A&A, 478, 353
Méndez-Abreu J., Simonneau E., Aguerri J. A. L., Corsini E. M., 2010, A&A, 521, A71
Minchev I., Famaey B., 2010, ApJ, 722, 112
Minniti D. et al., 2010, New A, 15, 433
Monachesi A., Bell E. F., Radburn-Smith D. J., Bailin J., de Jong R. S., Holwerda B., Streich D., Silverstein G., 2016, MNRAS, 457, 1419
Monachesi A. et al., 2019, MNRAS, 485, 2589
Mundy C. J., Conselice C. J., Duncan K. J., Almaini O., Häußler B., Hartley W. G., 2017, MNRAS, 470, 3507
Nataf D. M., Udalski A., Gould A., Fouqué P., Stanek K. Z., 2010, ApJ, 721, L28
Noguchi M., 1987, MNRAS, 228, 635
Okamoto T., 2013, MNRAS, 428, 718
Pakmor R., Springel V., 2013, MNRAS, 432, 176
Pakmor R., Marinacci F., Springel V., 2014, ApJ, 783, L20
Pakmor R., Springel V., Bauer A., Mocz P., Munoz D. J., Ohlmann S. T., Schaal K., Zhu C., 2016, MNRAS, 455, 1134
Pillepich A., Madau P., Mayer L., 2015, ApJ, 799, 184
Planck Collaboration XVI, 2014, A&A, 571, A16
Rodriguez-Gomez V. et al., 2017, MNRAS, 467, 3083
Romano-Díaz E., Shlosman I., Heller C., Hoffman Y., 2008, ApJ, 687, L13
Rosito M. S., Tissera P. B., Pedrosa S. E., Rosas-Guevara Y., 2019, A&A, 629, A37
Roškar R., Teyssier R., Agertz O., Wetzstein M., Moore B., 2014, MNRAS, 444, 2837
Saha K., 2015, ApJ, 806, L29
Saha K., Martinez-Valpuesta I., Gerhard O., 2012, MNRAS, 421, 333
Sales L. V., Navarro J. F., Theuns T., Schaye J., White S. D. M., Frenk C. S., Crain R. A., Dalla Vecchia C., 2012, MNRAS, 423, 1544
Sanders R. H., Huntley J. M., 1976, ApJ, 209, 53
Sawala T. et al., 2016, MNRAS, 457, 1931
Schaye J. et al., 2015, MNRAS, 446, 521
Searle L., Zinn R., 1978, ApJ, 225, 357
Sellwood J. A., Binney J. J., 2002, MNRAS, 336, 785
Sersic J. L., 1968, Atlas de Galaxias Australes, Observatorio astronmico, Cordoba, Argentina
Shen J., Rich R. M., Kormendy J., Howard C. D., De Propris R., Kunder A., 2010, ApJ, 720, L72
Simpson C. M., Grand R. J. J., Gómez F. A., Marinacci F., Pakmor R., Springel V., Campbell D. J. R., Frenk C. S., 2018, MNRAS, 478, 548
Springel V., 2010, MNRAS, 401, 791
Springel V., Hernquist L., 2003, MNRAS, 339, 289
Springel V., Di Matteo T., Hernquist L., 2005, MNRAS, 361, 776
Springel V. et al., 2008, MNRAS, 391, 1685
Tadaki K.-i. et al., 2017, ApJ, 834, 135
Tissera P. B., White S. D. M., Scannapieco C., 2012, MNRAS, 420, 255
Tissera P. B., Machado R. E. G., Carollo D., Minniti D., Beers T. C., Zoccali M., Meza A., 2018, MNRAS, 473, 1656
Vogelsberger M., Genel S., Sijacki D., Torrey P., Springel V., Hernquist L., 2013, MNRAS, 436, 3031
Wang L., Dutton A. A., Stinson G. S., Macciò A. V., Penzo C., Kang X., Keller B. W., Wadsley J., 2015, MNRAS, 454, 83
Wang L. et al., 2019, MNRAS, 482, 5477
Wetzel A. R., Hopkins P. F., Kim J.-h., Faucher-Giguère C.-A., Kereš D., Quataert E., 2016, ApJ, 827, L23
White S. D. M., Rees M. J., 1978, MNRAS, 183, 341
Zolotov A., Willman B., Brooks A. M., Governato F., Brook C. B., Hogg D. W., Quinn T., Stinson G., 2009, ApJ, 702, 1058

APPENDIX A: TWO-COMPONENT DECOMPOSITION OF SURFACE BRIGHTNESS PROFILES

Here we show the two-component decomposition of surface brightness profiles of the Auriga simulations. Surface brightness profiles were computed with the simulations as seen face-on, in concentric annuli of 500 pc wide, centred in the coordinate origin, defined as the most bound dark matter particle of each simulation. We use a non-linear least-square method to fit the sum of an exponential profile and a Sérsic model (Sersic 1968) which in terms of intensity reads

$$I(r) = I_{\rm e} \exp\left\{ -b_n \left[(r/r_{\rm eff})^{1/n} - 1 \right] \right\} + I_0 \exp\left[-(r/R_{\rm scale}) \right], \quad \text{(A1)}$$

where $r_{\rm eff}$ is the effective radius that encloses half of the total light of the Sérsic model, $I_{\rm e}$ is the intensity of the bulge component at $r_{\rm eff}$, n is the Sérsic index, I_0 is the central intensity of the disc component, and $R_{\rm scale}$ is the disc scale radius. b_n is such that $\Gamma(2n) = 2\gamma(2n, b_n)$, where Γ is the complete gamma function. The intensity is later converted into surface brightness to perform the fit. The fit of the surface brightness profile is limited to the optical radius as in G2017, who performed a similar fit to the mass density profile, following Marinacci et al. (2014). The fitting procedure was performed following Fisher & Drory (2008). In their work, surface brightness excesses due to features like bars, lenses, rings, and bright spiral structures are not taken into account in the fitting procedure. The central nuclei is also excluded from their fits. In the following, we exclude from our analysis the points in the surface brightness profile where the bar and other features, like spiral arms and rings are conspicuous. These surface brightness excesses are considered deviations from the smooth surface brightness profile assumed by our model (equation A). However, we do not exclude the central nuclei because the resolution of the simulations does not allow us to separate this component from the underlying peak of surface brightness. Thus, the total magnitudes of the Aurga bulges may be overestimated compared with the observed ones. In Figs A1 and A2 we show the surface brightness profiles of the Auriga simulations. The data used in the fit are shown with black filled circles and those excluded from the analysis with black empty circles. The fitted function is shown with a black line and the corresponding Sérsic and exponential profiles are shown with dotted and dashed lines, respectively.

In order to study the robustness of this method, we compare in Fig. A3 the Sérsic index and $r_{\rm eff}$ obtained when excluding points in the fitting procedure and those obtained using all the available points. We found that effective radii present small differences when using different fitting procedures, showing lower values, in general, when deviations from the smooth model are included in the fitting of the surface brightness profiles. Sérsic indexes also present differences when adopting different methods to fit the surface brightness profiles, but none of them is larger than $n = 2$ and none of the conclusions drawn in this work are affected by the fitting method used.

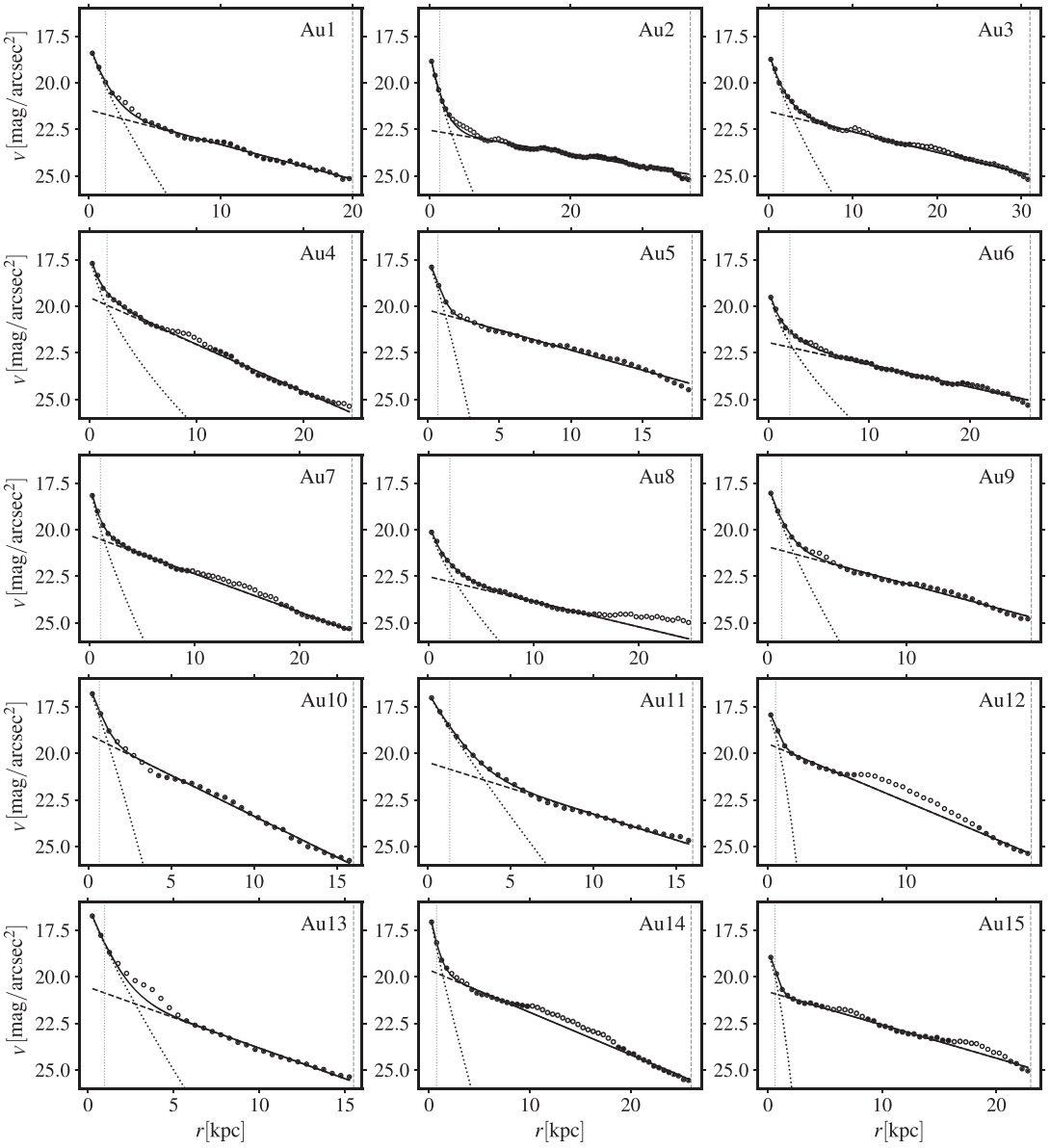

Figure A1. Bulge-disc decompositions of all the Auriga simulations from surface brightness fits that simultaneously fits a Sérsic profile and an exponential profile. Features in the surface brightness profiles due to bars, spiral structure, and rings, which deviate from the smooth nature of the model described by the sum of a Sérsic model (shown as dotted line) and an exponential profile (shown as dashed line), are excluded from the fit. We show with empty circles the values excluded from the fitting procedure. The vertical dotted line indicates the effective radius of the bulge component. The dashed vertical line indicates the optical radius of the simulation.

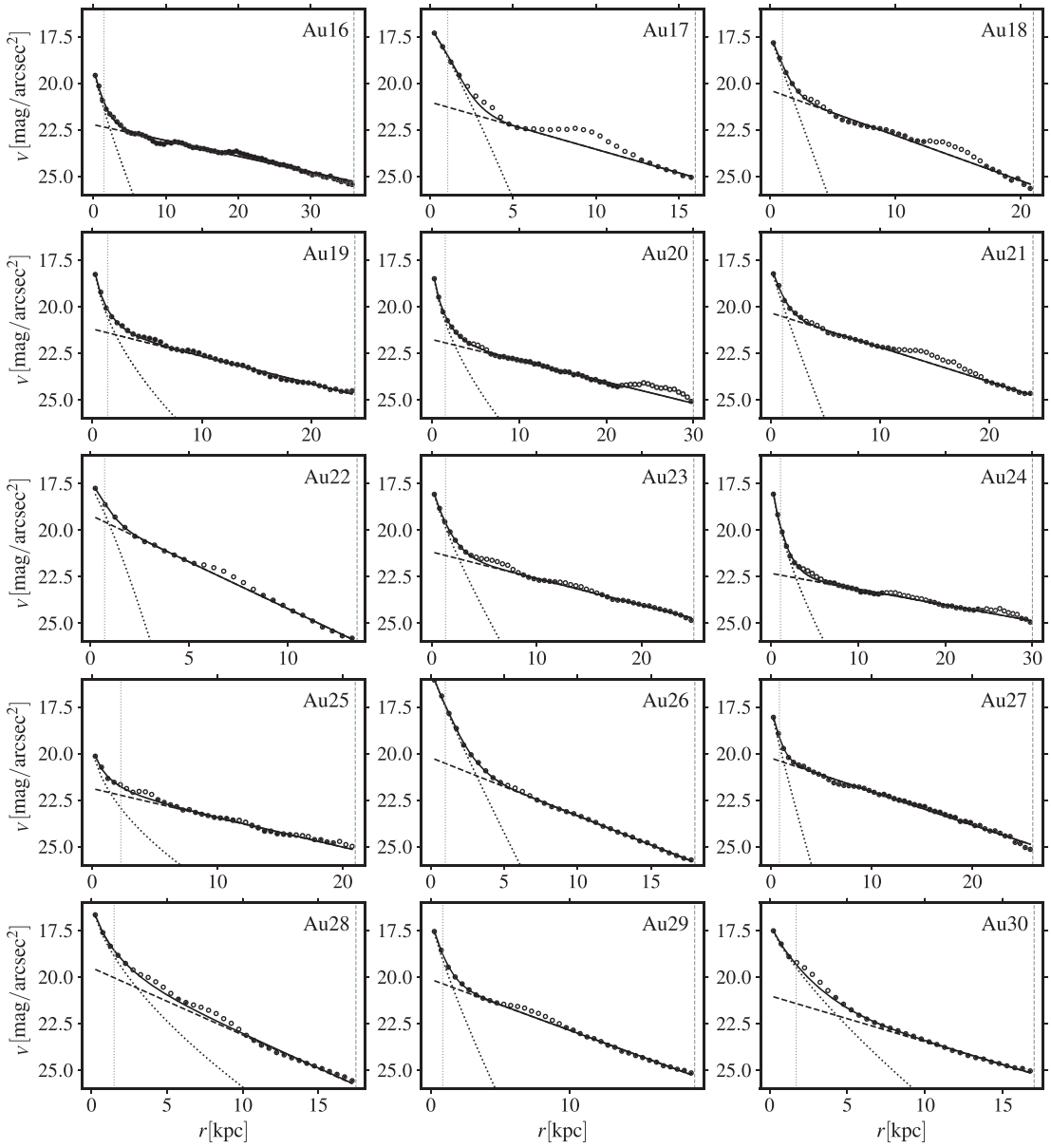

Figure A2. Same as in Fig. A1, but for Au16–Au30.

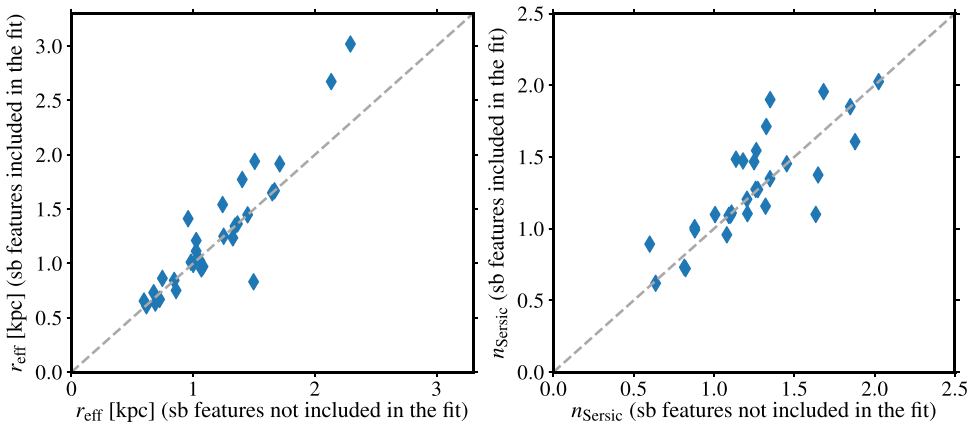

Figure A3. *Left*: Comparison of the effective radius of Auriga simulations obtained when surface brightness (sb) features are excluded from the fit and when they are not excluded from the fit. The dashed line indicates a 1:1 correlation. *Right*: Same as in the left-hand panel, but comparing the Sérsic index.

This paper has been typeset from a TEX/LATEX file prepared by the author.